






Viscoelastic Worthington jets and droplets produced by bursting bubbles

Ayush Dixit¹ , Alexandros Oratis^{1,2} , Konstantinos Zinelis^{3,4} ,
Detlef Lohse^{1,5}  and Vatsal Sanjay¹ 

¹Physics of Fluids Group, Max Planck Center for Complex Fluid Dynamics, Department of Science and Technology, and J. M. Burgers Centre for Fluid Dynamics, University of Twente, P.O. Box 217, Enschede, 7500 AE, The Netherlands

²Department of Chemical Engineering, Delft University of Technology, Delft 2629 HZ, The Netherlands

³Department of Chemical Engineering, Imperial College London, London SW7 2AZ, UK

⁴Department of Chemical Engineering, Massachusetts Institute of Technology, Cambridge, MA 02139, USA

⁵Max Planck Institute for Dynamics and Self-Organization, Am Fassberg 17, Göttingen 37077, Germany

Corresponding authors: Ayush Dixit, a.k.dixit@utwente.nl; Alexandros Oratis, a.t.oratis@tudelft.nl; Konstantinos Zinelis, zinelis@mit.edu; Detlef Lohse, d.lohse@utwente.nl; Vatsal Sanjay, vatsalsanjay@gmail.com

(Received 9 August 2024; revised 24 February 2025; accepted 24 February 2025)

Bubble bursting and subsequent collapse of the open cavity at free surfaces of contaminated liquids can generate aerosol droplets, facilitating pathogen transport. After film rupture, capillary waves focus at the cavity base, potentially generating fast Worthington jets that are responsible for ejecting the droplets away from the source. While extensively studied for Newtonian fluids, the influence of non-Newtonian rheology on this process remains poorly understood. Here, we employ direct numerical simulations to investigate the bubble cavity collapse in viscoelastic media, such as polymeric liquids. We find that the jet and drop formations are dictated by two dimensionless parameters: the elastocapillary number Ec (the ratio of the elastic modulus and the Laplace pressure) and the Deborah number De (the ratio of the relaxation time and the inertio-capillary time scale). We show that, for low values of Ec and De , the viscoelastic liquid adopts a Newtonian-like behaviour, where the dynamics is governed by the solvent Ohnesorge number Oh_s (the ratio of visco-capillary and inertio-capillary time scales). In contrast, for large values Ec and De , the enhanced elastic stresses completely suppress the formation of the jet. For some cases with intermediate values of Ec and De , smaller droplets are produced compared with Newtonian fluids, potentially enhancing aerosol dispersal. By mapping the phase space spanned by Ec , De and Oh_s , we reveal three distinct flow regimes: (i) jets forming droplets, (ii) jets without droplet formation and (iii) absence of

jet formation. Our results elucidate the mechanisms underlying aerosol suppression versus fine spray formation in polymeric liquids, with implications for pathogen transmission and industrial processes involving viscoelastic fluids.

Key words: viscoelasticity

1. Introduction

Bubbles in liquids (Lohse 2018) – from oceans (Deike 2022) and volcanoes (Gonnermann & Manga 2007) to cosmetic gels (Lin 1970; Daneshi & Frigaard 2024) and champagne (Liger-Belair 2012; Mathijssen *et al.* 2023) – rise due to buoyancy and reach the liquid–gas interface, where they sit as the intervening liquid film drains (figure 1*a*–i, Lhuissier & Villermaux 2012; Bartlett *et al.* 2023). Upon film rupture, numerous tiny droplets, known as film droplets, scatter over the free surface (Lhuissier & Villermaux 2012; Villermaux, Wang & Deike 2022), leaving a high-energy bubble cavity (figure 1*a*–ii, Woodcock *et al.* 1953; Knelman, Dombrowski & Newitt 1954; Mason 1954). The subsequent collapse of this cavity is driven by surface tension. This process involves rim retraction (Taylor 1959; Culick 1960; Sanjay *et al.* 2022) that generates capillary waves (Eggers, Sprittles & Snoeijer 2025). These waves propagate along the cavity, converging at its base to create an inertial flow focusing (Gordillo & Rodríguez-Rodríguez 2019; Gordillo & Blanco-Rodríguez 2023) that forms a Worthington jet (Worthington 1877, 1908; Stuhlman Jr 1932; Lohse *et al.* 2004; Sanjay 2022) that features large strain rates (Sen *et al.* 2024). The jet may fragment into droplets through end-pinching and the Rayleigh–Plateau instability (Lord Plateau 1873; Rayleigh 1878; Stone & Leal 1989; Keller, King & Ting 1995; Ghabache & Séon 2016; Walls, Henaux & Bird 2015). These jet droplets, typically larger and faster than the initial film droplets, play a crucial role in transporting dissolved substances to the atmosphere (Berny *et al.* 2020; Villermaux *et al.* 2022; Dubitsky *et al.* 2023*a*). The dynamics of bubble bursting has far-reaching implications across various domains. These include the transfer of pathogens from contaminated water to air (Bourouiba 2021), the transport of dissolved salt from seawater to the atmosphere, where salt particles act as cloud condensation nuclei (Dubitsky *et al.* 2023*b*; de Leeuw *et al.* 2011), and the dynamics in bioreactors containing animal cells (Boulton-Stone & Blake 1993). The unique capacity of ejected droplets to transport diverse species underscores the importance of comprehending the complete dynamics that dictates their formation. Ever since the first documented study of Stuhlman Jr (1932), advanced experiments and simulations have extensively characterised the rich dynamics of bursting bubbles. Key metrics include ejected drop heights (Stuhlman Jr 1932), sizes (Kientzler *et al.* 1954; Deike *et al.* 2018; Berny *et al.* 2020, 2021; Blanco-Rodríguez & Gordillo 2020; Villermaux *et al.* 2022) and velocities (Deike *et al.* 2018; Gordillo & Rodríguez-Rodríguez 2019; Sanjay, Lohse & Jalaal 2021; Gordillo & Blanco-Rodríguez 2023).

MacIntyre (1972) revealed internal liquid flow using dye and attempted to understand the drop composition, which was finally explained by direct numerical simulations (DNSs) of Dubitsky *et al.* (2023*a*). Furthermore, Dasouqi, Ghossein & Murphy (2022) demonstrated atmospheric flow patterns using smoke-filled bubbles, which were detailed numerically by Singh & Das (2021). Although shadowgraphy techniques limit most experimental studies, X-ray imaging has captured the travelling capillary wave dynamics, providing crucial validation for DNS results (Lee *et al.* 2011). These advancements have significantly enhanced our understanding of bubble bursting at the Newtonian liquid–gas interface across various scales and applications. Indeed, for a bubble of radius R_0 surrounded by a

liquid with viscosity, density and surface tension η_s , ρ_s and γ , the interplay of capillarity, viscosity and gravity governs the bubble cavity collapse. Correspondingly, the key control parameters of this process are the solvent Ohnesorge number

$$Oh_s = \frac{\eta_s}{\sqrt{\rho_s \gamma R_0}}, \quad (1.1)$$

and the Bond number

$$Bo = \frac{\rho_s g R_0^2}{\gamma}. \quad (1.2)$$

Here, g is the acceleration due to gravity. The solvent Ohnesorge number Oh_s exemplifies the dimensionless viscosity of the surrounding medium, significantly influencing the capillary wave dynamics, determining its damping and overall viscous dissipation, while the Bond number Bo affects the initial cavity shape and the hydrostatic pressure differences (Bergmann *et al.* 2006, 2009; Walls *et al.* 2015; Lohse 2018). In this study, we will focus our attention on the limiting case of very small bubbles with $Bo = 0.001$, for which the bubbles can be approximated as spheres (figures 1*a*, Toba 1959; Princen 1963; Lhuissier & Villermaux 2012). For the Newtonian cases, Appendix A summarises the key results, including the effect of Oh_s on the bubble-busting dynamics. For the influence of gravity on the shape and consequently the overall dynamics of Newtonian fluids, we refer the readers to Toba (1959), Princen (1963), Walls *et al.* (2015), Krishnan, Hopfinger & Puthenveetil (2017) and Deike *et al.* (2018).

Given the potential for jet drops to transport pathogens or pollutants into the atmosphere, strategies to prevent their generation are pertinent. Recent studies unsurprisingly show that non-Newtonian effects, particularly that viscoplasticity and viscoelasticity, can suppress jet drop production (Sanjay *et al.* 2021; Sen *et al.* 2021; Ji *et al.* 2023; Rodríguez-Díaz *et al.* 2023). While computational studies have successfully reproduced experimental observations, such as elasticity-induced droplet suppression (Balasubramanian *et al.* 2024; Cabalgante-Corrales *et al.* 2025), the full impact of these effects on the bubble-bursting dynamics remains elusive. In this paper, we answer the question: How does the viscoelasticity influence the observed regimes? What underlying physics governs the transitions between these regimes? Advancements in solving nonlinear constitutive equations for highly deformed interfacial flows of viscoelastic fluids have been made possible by techniques like the log-conformation method (Fattal & Kupferman 2004) and the square-root conformation method (Balci *et al.* 2011). Originally developed for single-phase flows, these methods have been extended to multiphase flows (Fraggedakis *et al.* 2016; López-Herrera *et al.* 2019; Varchanis & Tsamopoulos 2022; França *et al.* 2024; Zinelis *et al.* 2024), facilitating more comprehensive investigations into this topic.

Viscoelastic media differ from viscous Newtonian liquids in their rheological properties, exhibiting both viscous and elastic stresses when deformed due to the presence of dissolved polymers. These polymeric effects are characterised by two material properties: the elastic modulus G that characterises the strength of the dissolved polymers by relating the strain with the additional polymeric stresses in the system, and the relaxation time scale λ that characterises the memory of the system as it is a measure of the time scale at which the additional polymeric stresses in the system vanish. When non-dimensionalising these properties, we obtain two further non-dimensionalised control parameters, namely, the elastocapillary number

$$Ec = \frac{GR_0}{\gamma}, \quad (1.3)$$

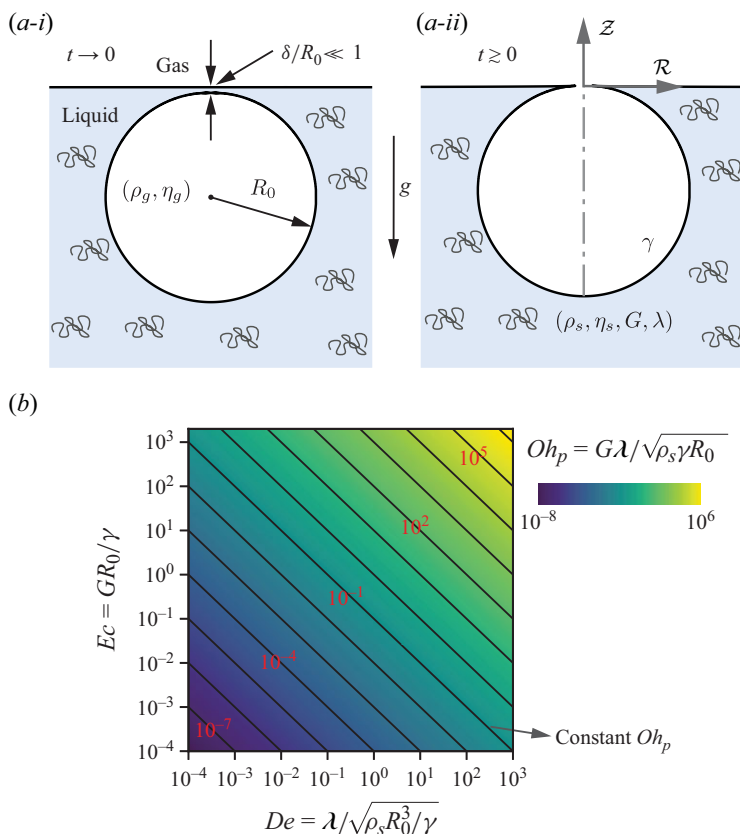


Figure 1. (a-i) A bubble with radius R_0 rests close to the liquid–gas interface, separated from it by a thin liquid film of thickness $\delta \ll R_0$. The surrounding viscoelastic medium is characterised by density ρ_s , solvent viscosity η_s , elastic modulus G and relaxation time λ . The gas has density ρ_g and viscosity η_g . (a-ii) Film rupture creates an axisymmetric cavity, which we study in this work. (b) Apart from the solvent Ohnesorge number $Oh_s = \eta_s/\sqrt{\rho_s \gamma R_0}$ and the Bond number $Bo = \rho_s g R_0^2/\gamma$, the presence of polymers introduces two additional parameters, namely the elastocapillary number $Ec = GR_0/\gamma$ (1.3) and the Deborah number $De = \lambda/\sqrt{\rho_s R_0^3/\gamma}$ (1.4). To explore the dynamics, we move across the entire Ec – De phase space. Often, the polymeric Ohnesorge number $Oh_p = G\lambda/\sqrt{\rho_s \gamma R_0} = Ec \times De$ (1.5) based on polymeric viscosity is also used to describe the influence of polymers.

comparing the elastic modulus with the Laplace pressure scale, and the Deborah number

$$De = \frac{\lambda}{\sqrt{\rho_s R_0^3/\gamma}}, \quad (1.4)$$

comparing the relaxation time of the additional stresses with the process time scale, i.e. the inerticapillary time scale $\tau_\gamma = \sqrt{\rho_s R_0^3/\gamma}$. Additionally, we also introduce the polymeric viscosity $\eta_p = G\lambda$ based on dimensional arguments, which can be normalised with the inerticapillary scales to give the polymeric Ohnesorge number (figure 1b)

$$Oh_p = \frac{\eta_p}{\sqrt{\rho_s \gamma R_0}} = Ec \times De, \quad (1.5)$$

which is the product of Ec and De . We note here that Oh_p and Oh_s are related by

$$Oh_p = \frac{\eta_p}{\eta_s} Oh_s = c Oh_s, \quad (1.6)$$

where $c = \eta_p/\eta_s$ is the so-called concentration of the polymers (see e.g. Remmelgas, Singh & Leal 1999; Hinch, Boyko & Stone 2024).

Prior experimental studies have provided valuable insights into viscoelastic effects on the bubble-bursting dynamics. Early work by Cheny & Walters (1996) demonstrated dramatic modifications of Worthington jets through polymer addition, where even small concentrations ($c \sim 50$ ppm) reduced jet heights by an order of magnitude. More recently, Rodríguez-Díaz *et al.* (2023) demonstrated how even weakly viscoelastic polymer solutions (with relaxation times $\lambda \leq 50 \mu s$) can dramatically alter the bubble-bursting dynamics through both interfacial and bulk effects. They found that, at optimal polymer concentrations (≈ 25 ppm), interfacial effects enhanced the jet velocity by dampening short-wavelength capillary waves, while at higher concentrations, extensional thickening led to complete droplet suppression. The elastic stress buildup during jet formation was further elucidated by Cabalgante-Corrales *et al.* (2025), who supported the previous observation that droplet emission is completely suppressed for large enough relaxation times (jet Weissenberg number $Wi_j = \lambda v_j/R \geq 0.5$, where v_j is the characteristic velocity of the Worthington jet), while the jet velocity is primarily dictated by Oh_p . These experimental observations motivate our systematic computational investigation of the Oh_s - Ec - De phase space to uncover the fundamental mechanisms that govern viscoelastic bubble bursting. We refer readers to Appendix B for a representative summary of the different control parameters.

In this study, we investigate viscoelastic effects on the bubble-bursting dynamics by exploring the three-dimensional phase space of Oh_s , Ec and De , using volume of fluid-based finite volume simulations. Using the Oldroyd-B constitutive relation, we demonstrate that the addition of polymers significantly influences the overall dynamics, which is governed by the interplay of viscous and elastic effects. For systems with a permanent memory of the initial state and subsequent deformations, i.e. when the additional polymeric stresses are sustained throughout the process time scale ($De \rightarrow \infty$), the dimensionless elastic modulus dictates the dynamics and suppression of jet and drops. In contrast, for systems with poor memory of the initial state and subsequent deformation ($De \rightarrow 0$), the dynamics resembles that encountered in Newtonian liquids with an effective viscosity deduced using the slender elastic jet equations. Despite its simplicity, we note that the Oldroyd-B model has some crucial limitations. For instance, it cannot account for the shear-thinning behaviour of polymer solutions and it predicts the divergence of stresses for strong extensional flows (Alves, Oliveira & Pinho 2021; Yamani & McKinley 2023). Consequently, the Oldroyd-B model cannot accurately capture the final stages of filament thinning or the actual rupture of viscoelastic filaments, which may affect predictions of droplet detachment and fine aerosol formation. Nevertheless, we choose the Oldroyd-B model as its simplicity allows us to gain fundamental insight into the interplay between capillary, viscous and elastic forces during bubble bursting.

Building upon the extensive literature on viscoelastic flows, we extend these concepts to the specific case of bubble bursting. Previous research has explored viscoelastic phenomena in various contexts, including flow through nozzles and contractions (Chen 1991; Hinch 1993; Boyko, Hinch & Stone 2024), stability and breakup of viscoelastic jets (Middleman 1965; Goren & Gottlieb 1982; Bousfield *et al.* 1986; Chang, Demekhin & Kalaidin 1999; Anna & McKinley 2001; Pandey *et al.* 2021; Sen *et al.* 2024; Zinelis *et al.* 2024), coalescence and spreading of viscoelastic drops and bubbles (Bouillant *et al.* 2022;

Dekker *et al.* 2022; Oratis, Bertin & Snoeijer 2023) and oscillating bubbles in viscoelastic media (Oratis *et al.* 2024). Recent studies have also investigated elastoviscoplastic flows, incorporating viscous, elastic and plastic aspects (Putz & Burghlea 2009; Varchanis *et al.* 2019; Balasubramanian *et al.* 2024; França *et al.* 2024), further expanding our understanding of non-Newtonian liquids. We refer readers to reviews by Boggy (1979), Eggers (1997) and Yarin (1993) for comprehensive overviews of these topics. Our work applies the foundational knowledge developed in these works to elucidate how viscoelasticity alters the formation of Worthington jets and ejected droplets during bubble bursting, enhancing our understanding of this specific phenomenon.

This paper is organised as follows: § 2 presents the governing equations and numerical method. § 3 investigates the polymer influence on bubble bursting, focusing on systems with permanent ($De \rightarrow \infty$, § 3.1) and poor ($De \rightarrow 0$, § 3.2) memory. For both cases, we categorise the bursting bubble dynamics into distinct regimes and elucidate the transitions in § 4, where we generalise the results across systems where the memory of the initial conditions and subsequent deformations is gradually fading ($0 < De < \infty$). Finally, § 5 summarises our findings and suggests future research directions.

2. Numerical framework and problem description

2.1. Governing equations

We investigate the collapse of an open bubble cavity at the interface in a viscoelastic medium (of figure 1) using an axisymmetric domain with incompressible fluids. Length scales are normalised using the initial bubble radius giving $\mathcal{L} = \tilde{\mathcal{L}}R_0$ as characteristic length, and the time is normalised using the inertio-capillary time scale $\tau_\gamma = \sqrt{\rho_s R_0^3 / \gamma}$ giving $t = \tilde{t}\tau_\gamma$. These normalisations yield an inertio-capillary velocity scale $u_\gamma = \sqrt{\gamma / \rho_s R_0}$ for the velocity field $\mathbf{u} = \tilde{\mathbf{u}}u_\gamma$. Lastly, all stresses are normalised using the Laplace pressure scale, $\boldsymbol{\sigma} = \tilde{\boldsymbol{\sigma}}\sigma_\gamma$, where $\sigma_\gamma = \gamma / R_0$. Here, as usual, non-dimensionalised quantities are denoted with a tilde, although from here onwards, we drop the tilde, and all equations are thus dimensionless in the current section. Throughout the manuscript, we use the subscripts s , p and g to denote liquid solvent, polymer and gas, respectively. The governing mass and momentum conservation equations for the liquid phase read as

$$\nabla \cdot \mathbf{u} = 0, \text{ and} \quad (2.1)$$

$$\frac{\partial \mathbf{u}}{\partial t} + \nabla \cdot (\mathbf{u}\mathbf{u}) = -\nabla p + \nabla \cdot (\boldsymbol{\sigma}_s + \boldsymbol{\sigma}_p), \quad (2.2)$$

where the Newtonian contribution (coming from the solvent) $\boldsymbol{\sigma}_s$ is

$$\boldsymbol{\sigma}_s = 2Oh_s \mathcal{D}, \quad (2.3)$$

with $\mathcal{D} = (\nabla \mathbf{u} + (\nabla \mathbf{u})^T)/2$ representing the symmetric part of the velocity gradient tensor – equal to half of the rate-of-strain tensor. The non-Newtonian contribution $\boldsymbol{\sigma}_p$ arises from the presence of polymers in the fluid. We emphasise that, although we refer to $\boldsymbol{\sigma}_p$ as ‘polymeric stresses’ in the context of dilute polymer liquids, this concept extends to any deformable microstructure within the fluid that responds to flow (Saramito 2007; Snoeijer *et al.* 2020; Balasubramanian *et al.* 2024; França *et al.* 2024). To characterise the deformation of these microstructures, we introduce the conformation tensor \mathcal{A} , an order parameter that evolves from an initial identity state $\mathcal{A} = \mathcal{I}$ (figure 1*a-ii*). Here, we employ the Oldroyd-B model, which represents the simplest conformation tensor-based constitutive equation for viscoelastic fluids (Oldroyd 1950; Bird, Armstrong & Hassager 1977; Snoeijer *et al.* 2020; Stone, Shelley & Boyko 2023; Boyko & Stone 2024). This model

assumes a linear relationship between elastic stresses and polymeric deformation

$$\sigma_p = Ec (\mathcal{A} - \mathcal{I}), \quad (2.4)$$

where Ec is the elastocapillary number (1.3), representing the strength of the polymers analogous to a dimensionless elastic modulus. Note that, even though the polymeric stresses σ_p grow linearly with \mathcal{A} , the polymeric deformations \mathcal{A} can be highly nonlinear. Naturally, in the limit of $Ec = 0$, the polymeric stress would vanish, and the system will give a viscous Newtonian dictated by the solvent Ohnesorge number Oh_s (see (2.3)).

Additionally, the conformation tensor \mathcal{A} relaxes to its base state \mathcal{I} over time due to thermal effects. Once more, using the Oldroyd-B model, \mathcal{A} follows a linear relaxation law (i.e. the rate of change of \mathcal{A} in the Lagrangian frame is linear in \mathcal{A})

$$\overset{\nabla}{\mathcal{A}} = -\frac{1}{De} (\mathcal{A} - \mathcal{I}), \quad (2.5)$$

where

$$\overset{\nabla}{\mathcal{A}} \equiv \frac{\partial \mathcal{A}}{\partial t} + (\mathbf{u} \cdot \nabla) \mathcal{A} - \mathcal{A} \cdot (\nabla \mathbf{u}) - (\nabla \mathbf{u})^T \cdot \mathcal{A}, \quad (2.6)$$

is the frame-invariant upper convected Oldroyd derivative of second-rank tensor \mathcal{A} , and $De = \lambda/\tau_\gamma$ (defined in (1.4)) is the Deborah number, representing the ratio of the polymer relaxation time λ to the process time scale τ_γ . We note that, while the Oldroyd-B model is nonlinear in terms of the velocity field and its gradient, both the stress term and its relaxation law remain linear in \mathcal{A} . This characteristic contrasts with models such as the Giesekus model, which involves a quadratic term $\mathcal{A} \cdot \mathcal{A}$ (Giesekus 1982), or the finite extensible nonlinear elastic (FENE) models, which include a nonlinear term involving a finite-extensibility parameter L (Bird, Dotson & Johnson 1980). Therefore, the Oldroyd-B model is often referred to as ‘quasi-linear’ (Davoodi *et al.* 2018; Alves *et al.* 2021).

The Deborah number characterises the polymeric liquid’s memory. It is instructive to note that, in the limit of $De \rightarrow \infty$, polymeric liquids have permanent memory and the dissolved polymers undergo affine motion (see (2.5) and Snoeijer *et al.* 2020; Stone *et al.* 2023; Boyko & Stone 2024)

$$\overset{\nabla}{\mathcal{A}} = 0, \quad (2.7)$$

indicating that they follow the flow and deform according to the velocity field. In this limit, for finite Ec , the Oldroyd-B model is equivalent to the damped neo-Hookean model (also known as the Kelvin–Voigt model) for solids (Snoeijer *et al.* 2020). Conversely, at $De = 0$, polymeric liquids have no memory of their initial condition and subsequent deformations, relaxing immediately to the base state. For non-infinite Ec values, polymeric stresses vanish, resulting in a Newtonian response (2.4) governed by the solvent Ohnesorge number Oh_s (see (2.3)). It is, therefore, surprising that both $Ec = 0$ and $De = 0$ (figure 1b) represent Newtonian responses, irrespectively of the corresponding other parameter.

Equations (2.4) and (2.5) can be combined to get

$$De \overset{\nabla}{\sigma}_p + \sigma_p = 2Oh_p \mathcal{D}, \quad (2.8)$$

where $Oh_p = Ec \times De$ is the polymeric Ohnesorge number (1.5). Consequently, in the limit $De \rightarrow 0$ at fixed Oh_p (e.g. moving along constant Oh_p lines in figure 1b), the system exhibits a viscous Newtonian response with a total dimensionless viscosity of $Oh_s + Oh_p$.

The Oldroyd-B model, despite its widespread use due to its simplicity, fails to capture several important physical phenomena (Snoeijer *et al.* 2020). It is inadequate to describe shear-thinning behaviour in polymeric liquids (Yamani & McKinley 2023) and erroneously predicts unbounded stress growth in strong extensional flows (McKinley & Sridhar 2002; Eggers, Herrada & Snoeijer 2020). The numerical discretisation of Oldroyd-B (§ 2.2) also features an implicit stress regularisation due to the finite grid size (Renardy & Thomases 2021) – similar in spirit to the implicit slip regularisation of the contact line singularity (Afkhami *et al.* 2018; Fullana *et al.* 2024). These limitations can be addressed by incorporating finite polymer extension, for example, by increasing the effective Ec as the polymer approaches full extension (Hinch & Harlen 2021; Zinelis *et al.* 2024). Various extensions of the Oldroyd-B equations have been developed to account for such nonlinearity, either in (2.4) and (2.5) or in the solvent contribution in (2.3) (de Gennes 1974; Tanner 2000; McKinley & Sridhar 2002; Alves *et al.* 2021). In this study, we employ the Oldroyd-B model to include the two primary effects of the polymer addition: the additional stress (Ec) and polymeric liquid memory (De) (Snoeijer *et al.* 2020). Our aim is to provide a comprehensive understanding of the entire Ec – De parameter space (figure 1*b*). However, it is crucial to note that the Oldroyd-B model, while serving as a useful baseline, cannot accurately reproduce the finite-time breakup of viscoelastic filaments (Eggers *et al.* 2020) or the full complexity of interface rupture (Lohse & Villiermaux 2020). These limitations warrant caution when interpreting the final stages of jet thinning and droplet formation, particularly in scenarios involving strong polymer stretching.

2.2. Methods

We employ the open-source software Basilisk C (Popinet & collaborators 2013–2024; Popinet 2015) to solve the governing equations outlined in § 2.1. To solve the Oldroyd-B viscoelastic constitutive relation (2.8), Basilisk C uses the log-conformation method (Fattal & Kupferman 2004) implemented by López-Herrera *et al.* (2019) which has been used extensively at finite De (Turkoz *et al.* 2018, 2021). To explore the entire Ec – De parameter space (figure 1*c*), we have extended the log-conformation formulation to solve (2.4) and (2.5). In the spirit of Basilisk C, this code is detailed open source in Sanjay (2024). The rest of the governing equations are solved using the one-fluid approximation (Tryggvason, Scardovelli & Zaleski 2011), with surface tension incorporated as singular body force at the liquid–gas interface (Brackbill, Kothe & Zemach 1992). To account for the gas phase, in addition to the dimensionless parameters described in §§ 1 and 2.1, we maintain constant density and viscosity ratios of $\rho_r = \rho_g/\rho_s = 10^{-3}$ and $\eta_r = \eta_g/\eta_s = 2 \times 10^{-2}$, respectively. The liquid–gas interface is tracked using the volume of fluid (VoF) method, governed by the advection equation

$$\frac{\partial \Psi}{\partial t} + \nabla \cdot (\Psi \mathbf{u}) = 0, \quad (2.9)$$

where Ψ represents the VoF colour function. We implement a geometric VoF approach, reconstructing the interface at each time step and applying surface tension forces as singular forces (Brackbill *et al.* 1992; Popinet 2009)

$$f\gamma \approx \kappa \nabla \Psi, \quad (2.10)$$

with curvature κ calculated using the height-function method (Popinet 2018). The explicit treatment of surface tension imposes a time step constraint based on the smallest capillary

wave oscillation period (Popinet 2009). Yet another time step restriction, usually more relaxed than the surface tension one, comes from the explicit treatment of the polymeric stress term σ_p . We impose no-penetration and free-slip conditions at wall boundaries to avoid wall-shear effects, with outflow conditions at the top boundary to prevent droplet rebound. Pressure gradients are set to zero at domain boundaries for both liquid and gas phases.

The initial bubble shape is determined by solving the Young–Laplace equations for quasi-static equilibrium (Toba 1959; Princen 1963; Sanjay 2022; Villiermaux *et al.* 2022). While the shape’s asymmetry increases with the Bond number Bo , we focus on the limit $Bo \rightarrow 0$, setting $Bo = 0.001$ to regularise the singularity at the sphere–plane intersection. This results in a near-spherical initial cavity shape (figure 1*a-i*). We stress that, here, we assume that the bubble has resided at the liquid–gas interface for a duration far exceeding the polymeric medium’s relaxation time, ensuring that elasticity does not influence the initial configuration (Balasubramanian *et al.* 2024). During the bubble cap bursting, the film cap retracts almost instantaneously (once again, we neglect the influence of elasticity), after which the capillary waves are generated. As we are interested only in the bubble cavity collapse, the simulations begin with an open cavity without the thin cap (figure 1*a-ii*), as also done similarly in recent studies (Deike *et al.* 2018; Gordillo & Rodríguez-Rodríguez 2019; Sanjay *et al.* 2021). The computational domain spans $8R_0 \times 8R_0$, discretised using quadtree grids with adaptive mesh refinement (Popinet 2009). Error tolerances for the VoF colour function, curvature, velocity and order parameter \mathcal{A} are set to 10^{-3} , 10^{-6} , 10^{-3} and 10^{-3} , respectively.

In this work, following our earlier study (Sanjay *et al.* 2021), most simulations maintain a minimum grid size of $\Delta = R_0/512$, which dictates that, to get consistent results, 512 cells are required across the bubble radius while using uniform grids. We have also used an increased resolution ($\Delta = R_0/1024$ for high De cases and $\Delta = R_0/2048$ near transitions) as needed. These resolutions are consistent with previous studies by Berny *et al.* (2020, 2021) on bubble bursting and Turkoz *et al.* (2018, 2021) on visco-elastic thinning with a maximum level of resolution of 14 (for $\Delta = R_0/2048$ and domain size $L_0 = 8R_0$). We have carried out extensive grid independence studies to ensure that changing the grid size does not influence the results (see Appendix C). We refer the readers to Popinet (2015), Sanjay (2022) and Sanjay & Dixit (2024) for further details of the numerical method used in this work.

3. Influence of polymers

This section phenomenologically describes the influence of polymers on the bursting bubble process by investigating how varying the elastocapillary number Ec influences the formation of Worthington jets and droplet ejection. We focus on two limiting cases: polymeric solutions with permanent memory exhibiting affine motion ($De \rightarrow \infty$) and those with poor memory ($De \rightarrow 0$).

3.1. Polymeric liquids with permanent memory

We begin our analysis by considering the limit of $De \rightarrow \infty$, where the polymeric solutions feature affine motion (2.7) and maintain a permanent memory of their initial condition and subsequent deformations without relaxation during the process time scale. Figure 2 illustrates representative cases in viscoelastic media for $Oh_s = 0.025$ and varying elastocapillary numbers (Ec). The figure presents a temporal evolution of the interface profile (green line) alongside the velocity magnitude on the left and the trace of elastic stress σ_p on the right. Remarkably, despite all cases exhibiting a total Ohnesorge number

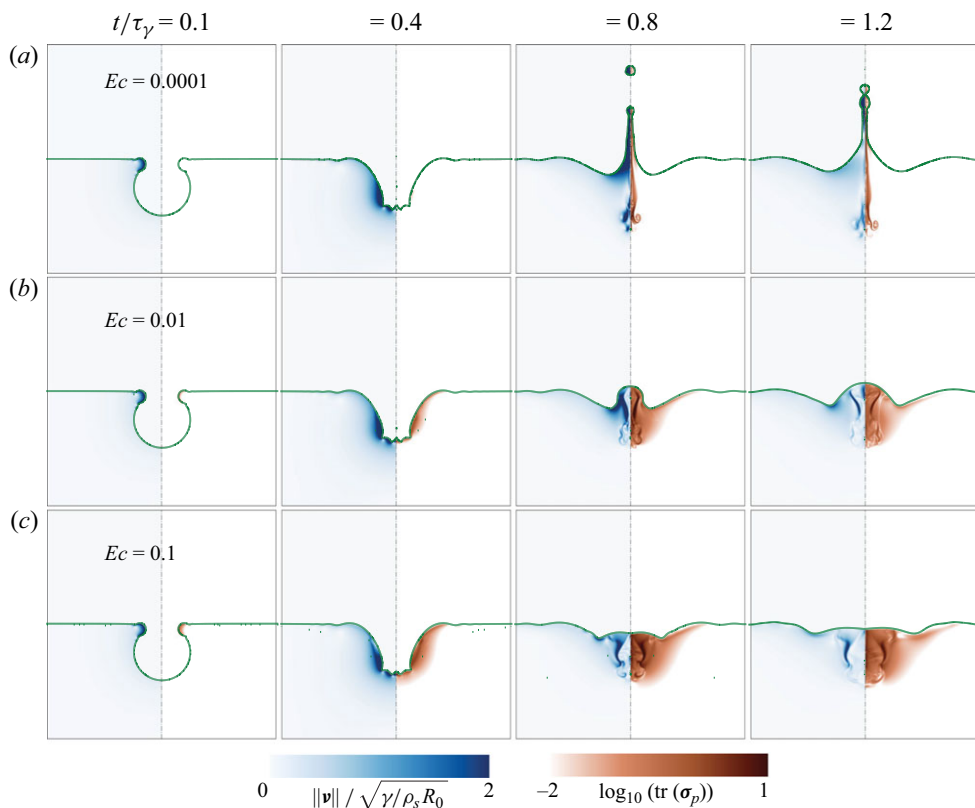


Figure 2. Temporal evolution of the bubble cavity collapse at $De \rightarrow \infty$ and $Oh_s = 0.025$ for $Ec = (a)$ 0.0001, (b) 0.01 and (c) 0.1. The colour scheme in the left panel of each snapshot represents the magnitude of the velocity field normalised by the inertio-capillary velocity, while the right panel of each snapshot shows the trace of the elastic stress σ_p that represents twice the elastic energy stored in polymeric deformations on a \log_{10} scale. See also the supplementary movies [SM1](#).

of infinity ($Oh_s + Oh_p \rightarrow \infty$), which typically implies highly viscous behaviour (see [figure 13](#)), low Ec scenarios demonstrate a dynamics qualitatively resembling Newtonian fluids. In these cases, capillary waves drive the collapse of a bubble cavity, converging at its bottom to form a Worthington jet that subsequently fragments into droplets (see [figure 2a](#)). Intuitively, the elastic stresses are concentrated near the axis of symmetry where the strain is maximum (Turkoz *et al.* 2018; Eggers *et al.* 2020). The process concludes within a finite time scale ($\sim \tau_\gamma$), resulting in a regular limit as $Ec \rightarrow 0$. As a result, the system's behaviour deviates gradually from the Newtonian case at $Ec = 0$, exhibiting a continuous transition as the elasticity increases. This absence of singularity contrasts with elastic Taylor–Culick-type retractions, where an infinite process time scale allows the elastic stresses to develop, leading to distinct behaviours for $Ec = 0$ and $Ec \rightarrow 0$ (Bertin *et al.* 2024), i.e. a singular limit.

We stress that in this limit, the jet breakup occurs due to finite grid resolution in our numerical code (Lohse & Villermaux 2020; Chirco *et al.* 2022; Kant *et al.* 2023). We cannot differentiate between a case of drop detachment from the jet or the case when they are still connected through a thin filament – also known as the beads-on-a-string structure (Clasen *et al.* 2006; Pandey *et al.* 2021; Hosokawa *et al.* 2023; Zinelis *et al.* 2024). Although current simulations fully resolve other aspects, they cannot resolve these finest

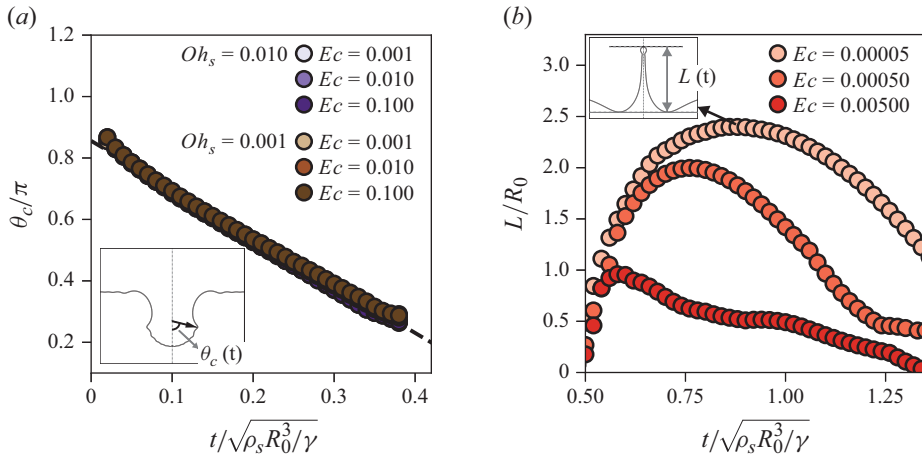


Figure 3. (a) Trajectory of the maximum curvature capillary wave parameterised using the angle $\theta_c(t)$ as depicted in the inset at $De \rightarrow \infty$ for different Oh_s and Ec . (b) Evolution of the jet length $L(t)$ at $Oh_s = 0.04$ and $De \rightarrow \infty$ for different Ec .

threads, which may have subgrid cell sizes depending on Ec . At higher grid resolutions, we expect to recover the beads-on-a-string configuration, as the Oldroyd-B model does not yield a finite time breakup singularity in the infinite De regime, instead converging to a finite filament (Turkoz *et al.* 2018, 2021; Eggers *et al.* 2020). To prevent infinite thread thinning, a nonlinear elastic model could also be employed (see § 2.1 for further discussions).

As Ec increases, we observe jet formation without droplet ejection (figure 2b). At higher Ec values, even jet formation is suppressed due to elevated elastic resistance (figure 2c). Notably, while polymeric effects significantly influence the dynamics after the convergence of capillary waves (figure 2, $t/\tau_\gamma = 0.8, 1.2$), the propagation of capillary waves (figure 2, $t/\tau_\gamma = 0.1, 0.4$) remains largely unaffected. Figure 3(a) quantifies the trajectories of these capillary waves across three orders of magnitude variation in Ec at two different Oh_s . The capillary wave speed is independent of both liquid and polymeric control parameters, mirroring the behaviour observed in Newtonian media (Gordillo & Rodríguez-Rodríguez 2019) and contrasting those for viscoplastic media (Sanjay *et al.* 2022). The independence of capillary wave speed on the polymeric control parameters has also been reported in experiments (Cabalgante-Corrales *et al.* 2025). Following capillary wave collapse, the Worthington jet initially elongates to a maximum length (L_{max}) before retracting. As shown in figure 3(b) for $Oh_s = 0.04$, L_{max} decreases with increasing Ec due to stronger resistive stresses.

Figure 4(a) presents a phase map of L_{max} , compiled from approximately 100 simulations. For Newtonian liquids, L_{max} peaks near $Oh_s \approx 0.03$, corresponding to the value of observed hydrodynamic singularities (Zeff *et al.* 2000; Lohse 2003; Eggers & Fontelos 2015; Yang, Tian & Thoroddsen 2020), before decreasing at higher Oh_s (Duchemin *et al.* 2002; Deike *et al.* 2018; Gordillo & Rodríguez-Rodríguez 2019). Jet formation ceases altogether beyond a critical value of $Oh_c = 0.11$ (Sanjay *et al.* 2021) (defined here when $L_{max} < 0.3R_0$). As Ec increases, viscoelastic effects become significant. The value of L_{max} decreases monotonically with Ec due to increased elastic resistance, with jet formation suppressed beyond $Ec = 0.086$. Unlike the non-monotonic relationship between L_{max} and Oh_s , where increasing Oh_s initially produces thinner and

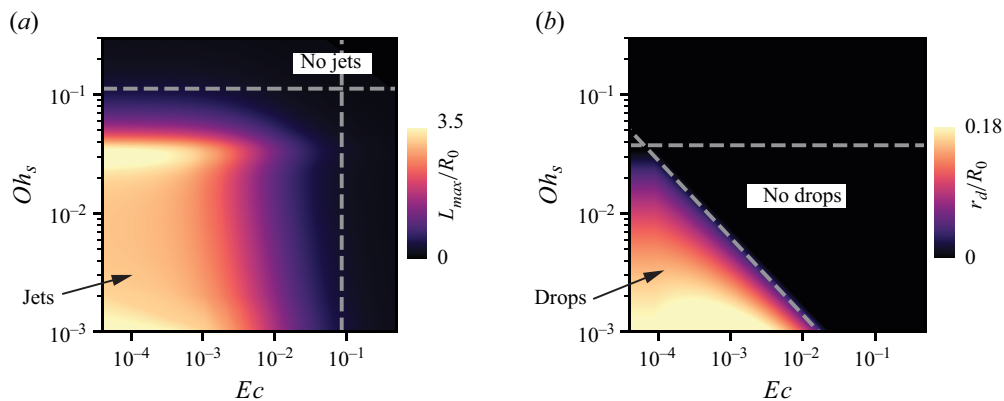


Figure 4. (a) The maximum jet length L_{max} at $De \rightarrow \infty$ in the Ec - Oh_s phase space, depicted by the colour map, where the lighter region corresponds to higher values. For the Newtonian liquid ($Ec \rightarrow 0$), the jetting transition occurs at $Oh_s = 0.11$, denoted by the horizontal dotted line. Due to the elastic effects, this transition occurs at $Ec = 0.086$, as depicted by the vertical dotted line. (b) The size of the first droplet at $De \rightarrow \infty$ in the Ec - Oh_s phase space. For the Newtonian liquid, the dropping transition is observed at $Oh_s = 0.0375$, denoted by the horizontal dotted line. Further, the transition due to elastic effects is very sensitive to Oh_s and is shown by the inclined dotted line.

faster jets, the $L_{max}(Ec)$ relationship remains consistently monotonic. Even the Oh_s -sensitive singular Worthington jets disappear with increasing Ec . Notably, the critical Ec values for these transitions appear to be largely independent of Oh_s , in contrast to the Oh_s -dependent behaviour observed in the Newtonian limit.

The emerging Worthington jet may eject multiple droplets. For Newtonian liquids, predictions, for the first droplets' size r_d are well understood (see Appendix A and Gañán-Calvo 2017; Blanco-Rodríguez & Gordillo 2020). Here, r_d decreases with Oh_s until $Oh_s \approx 0.0375$, beyond which the droplet breaks from the jet due to the Rayleigh–Plateau instability and falls downwards. Our analysis focuses on droplets propagating away from the source, excluding those with downward velocity upon breakup (observed in Newtonian media for $0.0375 < Oh_s < 0.045$). For elastic cases, despite unresolved filaments connecting droplets and jets, we have rigorously verified the convergence of the first droplet's size to at least 10% accuracy. Figure 4(b) illustrates a phase map of the first droplet's size r_d , revealing intriguing differences from the jet behaviour. While r_d follows the same trend with Oh_s observed at Newtonian limits and remains invariant of Ec below critical values, the critical Ec for droplet suppression differs from that of jet suppression. As the jet width is determined solely by Oh_s , independently of Ec , the first emerging droplet's size also remains independent initially. However, as Ec increases further, rising elastic stresses suppress droplet formation more abruptly than jet formation. The critical values Ec_d for the transition between jet formation with and without droplet breakup (dropping transition) are sensitive to Oh_s , with the critical Ec_d decreasing as Oh_s increases. This trend is in stark contrast with the transition from jet formation to jet suppression (jetting transition), where critical Ec values remain largely Oh_s -independent.

3.2. Polymeric liquids with poor memory

This section examines the dynamics in media with a poor memory of the initial conditions and subsequent deformations ($De \rightarrow 0$). For sufficiently small Deborah numbers De , the polymers relax rapidly, resulting in elastic stresses of the polymeric liquid that are considerably lower than those observed in cases where $De \rightarrow \infty$. The stress relaxation

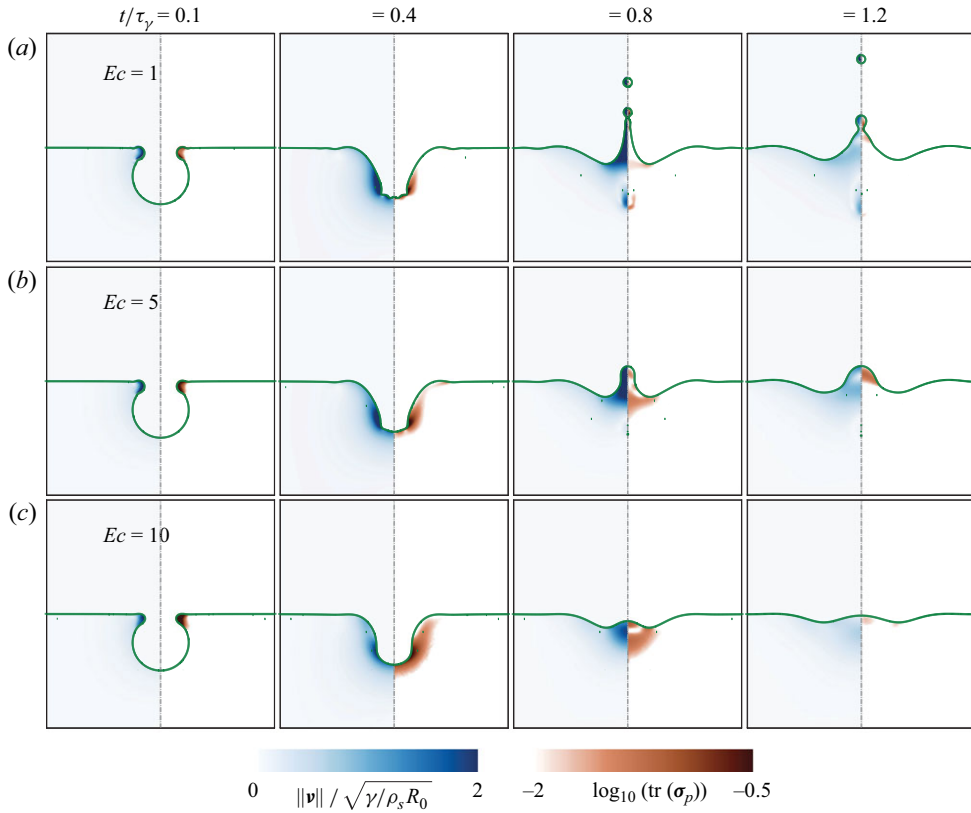


Figure 5. Temporal evolution of bubble cavity collapse at $De = 0.01$ and $Oh_s = 0.025$ for $Ec = (a) 1$, $(b) 5$ and $(c) 10$. The colour scheme in the left panel of each snapshot represents the magnitude of the velocity field normalised by the interfacial velocity, while the right panel of each snapshot shows the trace of the elastic stress σ_p that represents twice the elastic energy stored in polymeric deformations on a \log_{10} scale. See also the supplementary movies [SM2](#).

also results in the dissipation of elastic energy stored in stretched polymers. [Figure 5](#) illustrates representative cases for $De = 0.01$, showcasing three distinct regimes as a function of the elastocapillary number (Ec). The figure presents a temporal evolution of the interface profile (green line) alongside velocity magnitude on the left and the trace of elastic stress σ_p on the right for $Ec = 1, 5$ and 10 . For $Ec = 1$ ([figure 5a](#)), we observe a slender Worthington jet that forms a droplet. As Ec increases to 5 ([figure 5b](#)), the jet persists but fails to produce a droplet. At $Ec = 10$ ([figure 5c](#)), jet formation is completely suppressed, with the interface showing only slight deformations during cavity relaxation. The qualitative trends with respect to the elastocapillary number (Ec) remain consistent as compared with those in § 3.1. However, the critical Ec values for different regimes differ markedly from those observed at $De \rightarrow \infty$. Notably, jet formation and droplet production persist at $Ec = 1$ ([figure 5a](#)), despite this value being an order of magnitude higher than the critical Ec for the jetting transition at infinite De . This difference underscores the dependence of transition thresholds on De .

To further interpret the jetting dynamics and drop formation, [figure 6](#) presents phase maps illustrating the behaviour of maximum jet lengths (L_{max}) and first droplet sizes (r_d) for $De = 0.01$. [Figure 6\(a\)](#) shows L_{max} across a range of Ec and Oh_s values. For low Ec , L_{max} shows Newtonian-like Oh_s dependence. As Ec increases, L_{max}

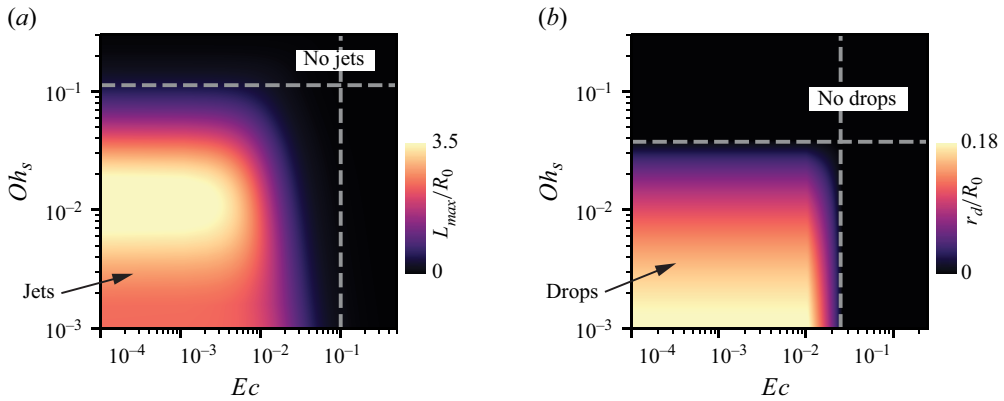


Figure 6. (a) The maximum jet length L_{max} at $De = 0.01$ in the Ec - Oh_s phase space, depicted by the colour map, where the lighter region corresponds to higher values. For the Newtonian liquid, the jetting transition occurs at $Oh_s = 0.11$, denoted by the horizontal dotted line. Due to the elastic effects, this transition occurs at $Ec = 9.3$, as depicted by the vertical dotted line. (b) The size of the first droplet at $De = 0.01$ in the Ec - Oh_s phase space. For the Newtonian liquid, the dropping transition is observed at $Oh_s = 0.0375$, denoted by the horizontal dotted line. Further, the Oh_s -independent transition due to elastic effects occurs at $Ec = 2.5$, as shown by the vertical dotted line.

decreases monotonically until jet formation ceases beyond an Oh_s -independent critical Ec_j , mirroring the infinite De limit behaviour. Figure 6(b) maps r_d , showing Ec -independent droplet sizes that are equal to values at the Newtonian limit until near the transition point, where droplet formation is suppressed. For $De \ll 1$, the critical Ec_d for the dropping transition exhibits minimal Oh_s -dependence, contrasting with the Oh_s -sensitive behaviour at infinite De . Comparing these results with the $De \rightarrow \infty$ limit reveals persistent fundamental regimes across different De values, but the transition thresholds are highly sensitive to the polymeric liquid's relaxation time. Critical Ec values for both jet and droplet suppression are significantly higher at low De compared with the infinite De limit, indicating that rapid relaxation of polymeric stresses allows jet and droplet formation at higher Ec values. This low De behaviour suggests an interplay between elastic and viscous effects, explored further in § 4.

4. Regime map

The bursting bubble dynamics in viscoelastic media exhibits distinct behaviour compared with Newtonian fluids. Our analysis reveals three well-defined regimes: (i) jets that form droplets, (ii) jets without droplet formation and (iii) complete suppression of jets. While viscoelasticity significantly modifies the jet dynamics, the capillary wave propagation prior to jet formation remains remarkably unaffected. This section explores the transitions between these regimes across the Ec - De phase space, extending our earlier analysis of the limiting cases $De \rightarrow \infty$ and $De \rightarrow 0$ from § 3.

4.1. Summary of the different regimes

The transitions between these regimes depend on both Ec and De , exhibiting markedly different characteristics in two limiting cases: $De \rightarrow \infty$ and $De \rightarrow 0$. Figure 7 maps these transitions in the elastocapillary–Deborah number (Ec – De) phase space, delineating the boundaries between droplet-forming jets and jets without droplets. Figure 8 complements this by illustrating the transition to complete jet suppression. Notably, the infinite De

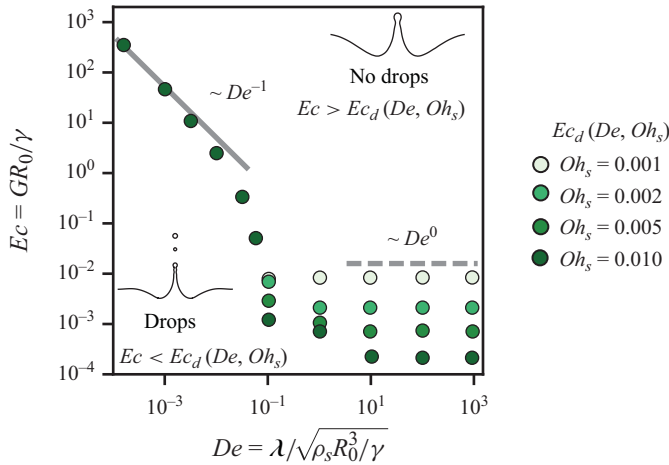


Figure 7. The elastocapillary–Deborah number (Ec – De) phase map delineating the transition between the regimes: (i) jets forming droplets and (ii) jets without droplet formation. The data points represent the critical elastocapillary number $Ec_d(De, Oh_s)$ at which this transition occurs. The transition behaviour exhibits distinct characteristics in different limits: as $De \rightarrow \infty$, the transition occurs at a constant Ec which is highly sensitive to Oh_s (see the grey dashed line showing $Ec_d \sim De^0$), while for $De \rightarrow 0$, the transition is Oh_s -independent and occurs at constant Oh_p (see the grey solid line showing $Ec_d \sim De^{-1}$, i.e. $Oh_{p,d} \sim De^0$).

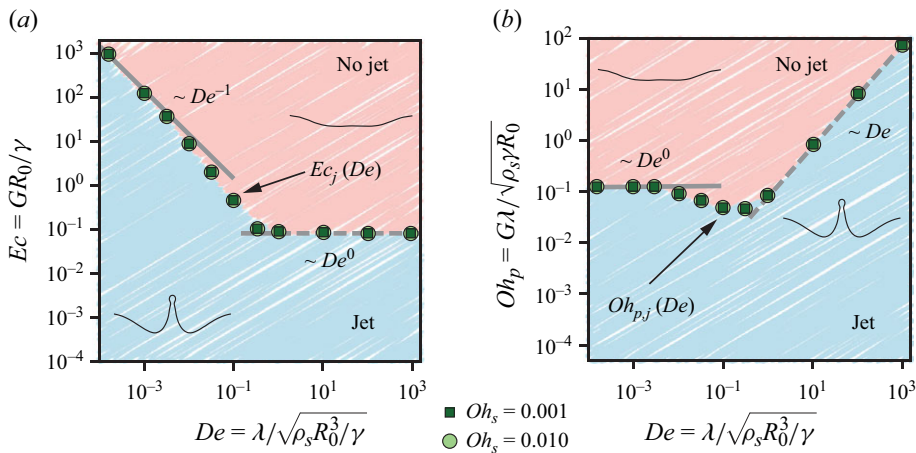


Figure 8. (a) The elastocapillary–Deborah number (Ec – De) and (b) the polymeric Ohnesorge–Deborah number (Oh_p – De) phase map delineating the transition between the regimes: (ii) jets without droplet formation and (iii) absence of jet formation. The data points represent the Oh_s -independent critical elastocapillary number $Ec_j(De)$ at which this transition occurs. The transition behaviour exhibits distinct characteristics in different limits: as $De \rightarrow \infty$, the transition occurs at a constant Ec (see grey dashed line showing $Ec_d \sim De^0$), while for $De \rightarrow 0$, the transition occurs at constant Oh_p (see grey solid line showing $Ec_d \sim De^{-1}$, i.e. $Oh_{p,d} \sim De^0$).

asymptotic behaviour extends down to $De \approx 1$, reflecting that polymers lack sufficient time to relax when relaxation times exceed the process time scale.

For polymeric liquids with long relaxation times ($De \gg 1$), we observe that:

- (i) the dropping transition occurs at $Ec_d(Oh_s)$, with strong Oh_s dependence (figures 4b and 7); and

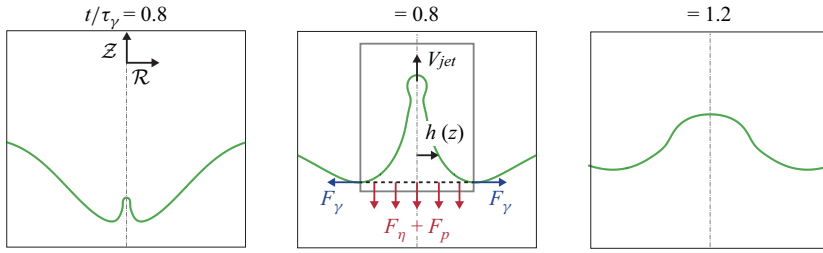


Figure 9. Temporal evolution of the Worthington jet for a representative case, where the jet emerges, reaches a maximum, and is pulled to merge with the liquid bath. The control volume contains the jet region, as shown by the region within the grey lines. Here, $h(z, t)$ is the width of the jet, which becomes h_{base} at the base of the jet. The capillary force at the jet base is $F_\gamma = \gamma(2\pi h_{base})$ that acts radially outwards. At the same time, the elastic and viscous stresses act at the base of the jet as $F_\eta + F_p = (\sigma_{\eta,base} + \sigma_{p,base})\pi h_{base}^2$.

(ii) the jetting transition occurs at $Ec_j \approx 0.086$, independent of Oh_s (figure 8a).

Conversely, for polymeric liquids with short relaxation times ($De \ll 1$), we find that both transitions are Oh_s -independent and occur at constant polymeric Ohnesorge number $Oh_p = Ec \times De$:

- (i) the dropping transition occurs at $Oh_{p,d} \approx 0.048$ (figure 7); and
- (ii) the jetting transition occurs at $Oh_{p,j} \approx 0.129$ (figure 8b).

These behaviours reflect fundamentally different physical mechanisms: at high De , depending on Oh_s , the medium behaves like an elastic solid ($Oh_s \rightarrow 0$) or Kelvin–Voigt solid (finite Oh_s). However, at low De , polymer addition manifests as an enhanced viscous effect characterised by Oh_p . The trend of dropping transition in the small De regime is qualitatively similar to recently reported experimental observation (Cabalgante-Corrales *et al.* 2025). Although, a quantitative comparison cannot be made due to significant differences in Bo . We further investigate the jetting transition using the slender jet equations in § 4.2 following similar approaches by Driessen *et al.* (2013), Gordillo, Onuki & Tagawa (2020), Zinelis *et al.* (2024) and Sen *et al.* (2024).

4.2. What sets the different transitions, and what do we learn from these transitions?

To understand the mechanisms governing bubble cavity collapse, we analyse the jet dynamics using a control volume approach (figure 9). Employing the slender jet approximation (Shi, Brenner & Nagel 1994; Driessen *et al.* 2013; Eggers & Fontelos 2015), given the small radial-to-axial length scale ratio, the vertical momentum equation for the jet reads

$$\rho_s \left(\frac{\partial v}{\partial t} + v \frac{\partial v}{\partial z} \right) = -\gamma \frac{\partial \kappa}{\partial z} + \frac{1}{h^2} \frac{\partial}{\partial z} \left[h^2 \left(3\eta_s \frac{\partial v}{\partial z} + G (\mathcal{A}_{zz} - 1) \right) \right]. \quad (4.1)$$

Here, $v(z, t)$ is the radially averaged jet velocity, and the shape of this jet is $h(z, t)$. We define a control volume containing the emerging jet that is always bounded by the inflection points at the interfaces, see figure 9(b). Integrating over this control volume (with differential volume element $d\Omega = \pi h(z, t)^2 dz$) yields the force balance (Trouton 1906)

$$\frac{d\mathcal{M}_{jet}}{dt} = 3\eta_s h^2 \frac{\partial v}{\partial z} \Big|_{base} + G h^2 (\mathcal{A}_{zz} - 1) \Big|_{base} = (\sigma_{\eta,base} + \sigma_{p,base}) \pi h_{base}^2, \quad (4.2)$$

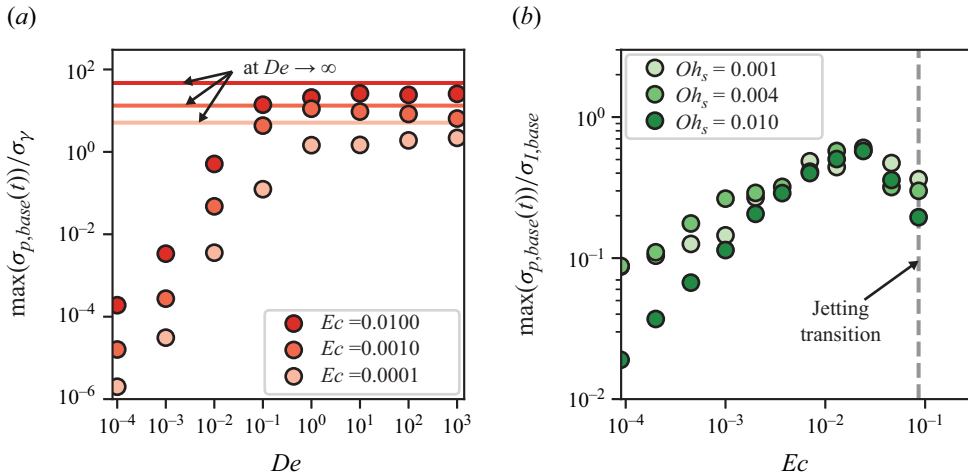


Figure 10. (a) Evolution of the maximum elastic stress at the jet base ($\max(\sigma_{p,base}(t))$), normalised by the Laplace pressure scale $\sigma_\gamma = \gamma/R_0$, as a function of De for different Ec at $Oh_s = 0.001$. Note that $Oh_p = Ec \times De$. (b) Comparison of the resistive elastic stress $\max(\sigma_{p,base}(t))$ in the high De regime ($\rightarrow \infty$) against the inertial stresses $\sigma_{I,base}$, plotted against Ec for different Oh_s .

where $\mathcal{M}_{jet}(t) = \int_{\Omega(t)} \rho_s v(z, t) \pi h(z, t)^2 dz$ denotes the momentum of the jet. The capillary stress (first term on the right-hand side of (4.1)) integral vanishes due to orthogonal interface intersection with the control volume (see Marchand *et al.* 2011; Munro 2019, pp. 16–21). We chose this control volume because of its vanishing integral feature. Furthermore, the integral of the second term on the right-hand side forms an exact integral which vanishes at the tip where it is zero owing to $h(z = L_{max}(t)) = 0$. Consequently, jet evolution depends solely on stresses at the base: viscous ($\sigma_{\eta,base}(t)$) and elastic ($\sigma_{p,base}(t)$). For relevant Oh_s values, $\sigma_{\eta,base}(t)$ is too weak to suppress the Worthington jet. Numerical simulations allow us to estimate $\sigma_{p,base}(t)$. As the capillary waves collapse, the base elastic stress reaches a global maximum, before decreasing again at later times. Jet formation occurs if inertial flow focusing is sufficiently strong at the peak elastic stress. We will now evaluate this competition for the two limits of De .

4.2.1. The limit of $De \rightarrow \infty$

Figure 10(a) shows that, for $De > 1$, the maximum elastic stress $\max(\sigma_{p,base}(t))$ reaches a plateau, dependent only on Ec . This De -independence coincides with the extent of infinite De asymptotes featured in the transitions discussed in § 4.1. The upper limit of elastic resistance competes with inertial flow focusing to inhibit jet formation. We quantify the inertial stresses at peak elastic stress using

$$\sigma_{I,base} = \frac{2}{h_{base}^2} \int_0^{h_{base}} \rho_s v^2 h dh, \quad (4.3)$$

where h_{base} is the jet width at its base (see figure 9). Figure 10(b) reveals that the ratio of elastic to inertial stresses is largely independent of Oh_s . As Ec increases, this ratio reaches a maximum beyond which jet suppression occurs. It is important to note that the apparent decrease in this stress ratio with increasing Ec and Oh_s near the jetting transition in figure 10(b) occurs due to a decrease in both the polymeric and inertial stresses in this region of the parameter space.

4.2.2. The limit of $De \rightarrow 0$

In the zero De limit, polymeric liquids exhibit additional viscous effects characterised by the polymeric Ohnesorge number Oh_p (also see § 4.1). The maximum elastic stress $\max(\sigma_{p,base}(t))$, when normalised by the Newtonian-like viscous stress $\sigma_{N,base}$, collapses for all Oh_p as $De \rightarrow 0$, where

$$\sigma_{N,base} = \frac{2}{h_{base}^2} \int_0^{h_{base}} G\lambda \frac{\partial v}{\partial z} h dh. \quad (4.4)$$

As De approaches unity, marking the onset of the infinite De asymptotic regime, the elastic stress scales as $\max(\sigma_{p,base}(t)) \sim De \times \sigma_{N,base}$. This scaling remarkably resembles that predicted by Boyko *et al.* (2024) for flow in a slowly varying contraction at the infinite De asymptote, despite significant geometric differences. While our study focuses on free surface flows and Boyko *et al.* (2024) examined contraction geometries, this unexpected similarity hints at a potentially universal behaviour near the infinite De asymptote. To further examine this intriguing connection, a similar closed-form De expansion for free surface flows is necessary. However, we caution that this scaling approach to the infinite De asymptote could be system-dependent (Hinch *et al.* 2024).

At zero De , the elastic stress reduces to a Newtonian-like viscous stress with polymeric viscosity η_p , yielding $\sigma_p \approx 2G\lambda\mathcal{D}$ for the Oldroyd-B rheology. The force balance in (4.2) becomes

$$\frac{d\mathcal{M}_{jet}}{dt} = (3\eta_s + 2G\lambda) h^2 \frac{\partial v}{\partial z} |_{base}, \quad (4.5)$$

which depicts the balance of jet inertia with viscous forces. Using characteristic scales for jet momentum $\mathcal{M}_{jet} \sim \rho V_{jet} h_{base}^3$, velocity gradient $\partial_z v \sim V_{jet}/\delta_\eta$ and time $\tau_i \sim h_{base}/V_{jet}$, the force balance yields

$$\rho V_{jet}^2 \sim \eta_{effective} \frac{V_{jet}}{\delta_\eta}. \quad (4.6)$$

Here, δ_η represents the viscous length scale and the effective viscosity is

$$\eta_{effective} = 3\eta_s + 2G\lambda. \quad (4.7)$$

Since polymers do not affect the flow before jet formation (§ 3), the jet Weber number remains constant at inception (Blanco-Rodríguez & Gordillo 2021)

$$We_{jet} = \frac{\rho V_{jet}^2 \delta_\eta}{\gamma} = \text{constant}. \quad (4.8)$$

Combining (4.6) and (4.8), we get

$$V_{jet} \sim \frac{\gamma}{\eta_{effective}}, \quad (4.9)$$

analogous to Newtonian media but with modified viscosity (Gordillo & Rodríguez-Rodríguez 2019; Blanco-Rodríguez & Gordillo 2020).

Figure 11(b) illustrates the jet velocity as a function of the effective Ohnesorge number

$$Oh_{effective} = 3Oh_s + 2Oh_p, \quad (4.10)$$

(reflecting (4.7)) at different De . We stress that the jet velocity varies in time (Deike *et al.* 2018; Sanjay *et al.* 2022; Gordillo & Blanco-Rodríguez 2023) and is maximum at its

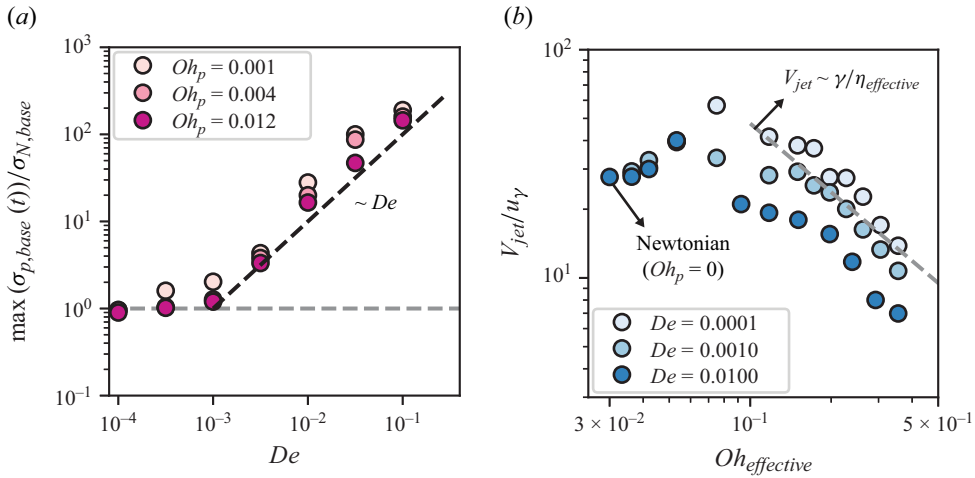


Figure 11. (a) Evolution of the maximum elastic stress at the jet base ($\max(\sigma_{p,base}(t))$), normalised by the Newtonian-like viscous stress $\sigma_{N,base}$ with viscosity $\eta_p = G\lambda$, as a function of De for different Oh_p at $Oh_s = 0.001$. The grey dashed horizontal line represents $\max(\sigma_{p,base}(t)) \approx \sigma_{N,base}$ while the black dashed line serves as a guide to the eye representing $\max(\sigma_{p,base}(t))/\sigma_{N,base} \sim De$. Note that $Ec = Oh_p/De$. (b) The variation of jet's tip velocity V_{jet} , normalised by the intercapillary velocity $u_\gamma = \sqrt{\gamma/\rho_s R_0}$, with $Oh_{effective} = 3Oh_s + 2Oh_p$ at different De and $Oh_s = 0.01$. The grey dashed line represents $V_{jet} \sim \gamma/\eta_{effective}$.

inception, which is the value that we report here. For sufficiently large $Oh_{effective}$ and small De , we recover the scaling predicted in (4.9). However, as De increases, the added elastic stresses cannot be directly substituted with Newtonian-like viscous stresses, and the underlying assumption fails, evident in the deviation of V_{jet} from the prediction.

On the other hand, for small $Oh_{effective}$, V_{jet} for all De closely matches the corresponding speed in Newtonian liquids, as observed in figure 11(b) for $Oh_p = 0$. As Oh_p increases, V_{jet} also increases, reaching a maximum before decreasing and following (4.9). Although the capillary wave speed remains unaffected in the polymeric medium, increasing Oh_p triggers elastic stresses in smaller-wavelength capillary waves, which are promptly dissipated due to small De . Consequently, improved flow focusing occurs as the strongest undamped capillary wave survives, thus increasing V_{jet} . This behaviour is analogous to the non-monotonicity observed and well understood for Newtonian liquids at small Oh_s (Duchemin *et al.* 2002; Deike *et al.* 2018; Gordillo & Rodríguez-Rodríguez 2019; Yang *et al.* 2020; Sanjay *et al.* 2022; Gordillo & Blanco-Rodríguez 2023), further supporting the observation that polymeric liquid exhibit a Newtonian-like viscous response in the zero De limit.

To further quantify this behaviour, figure 12(a) illustrates jet features at inception for different Oh_p at $De = 0.001$, while figure 12(b) shows jet radius as a function of Oh_p at different De . At small Oh_p , we observe that the jet radius maintains a value comparable to the Newtonian reference case (figure 12a: $Oh_p = 0, 0.005$). This behaviour is consistent with the $De \rightarrow 0$ limit, where polymeric additives primarily contribute enhanced effective viscosity. Since the jet radius determines the resulting drop size (Gañán-Calvo 2017; Blanco-Rodríguez & Gordillo 2020), this independence of jet radii in the low Oh_p regime suggests minimal variation in droplet size distribution compared with Newtonian cases. As Oh_p increases, we observe a pronounced reduction in jet width until reaching $Oh_{p,c} \approx 0.017$ (figure 12a: $Oh_p = 0.013, 0.018$). At this critical value, the system transitions to a bubble entrainment regime (figure 12a: $Oh_p = 0.018, 0.025$

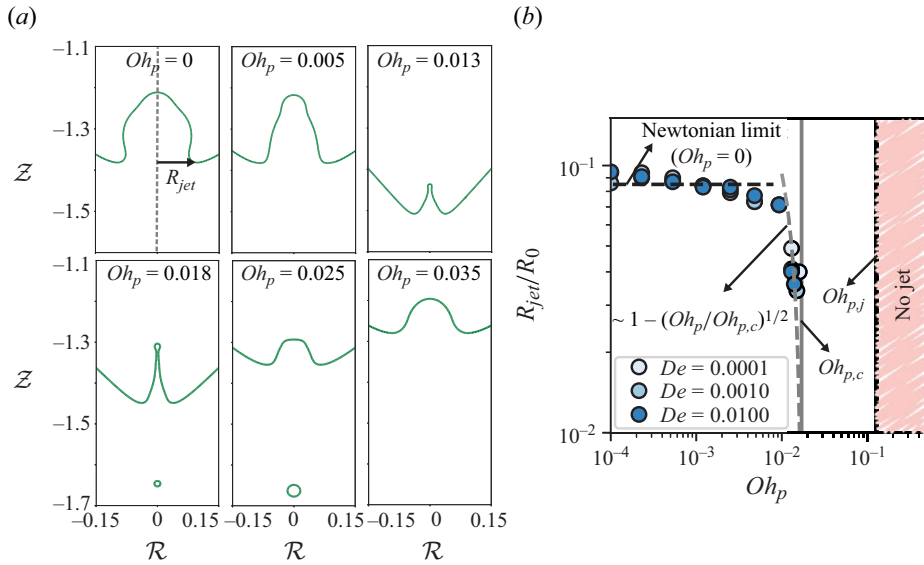


Figure 12. The capillary waves focus and collapse at the bottom of the cavity. (a) The inception of the jet after the collapse at different Oh_p at $De = 0.001$ and $Oh_s = 0.01$. The radius of the jet at the base R_{jet} decreases with Oh_p until $Oh_{p,c} = 0.017$, beyond which bubbles are entrained and the jet radius increases. (b) Radius of jet R_{jet} with Oh_p at $Oh_s = 0.01$ and different De . Here, R_{jet} remains close to the value at the Newtonian limit $Oh_p = 0$, and decreases sharply as it approaches $Oh_{p,c}$. Beyond $Oh_{p,j}$ jets are no longer observed.

Gordillo & Rodríguez-Rodríguez 2019; Blanco-Rodríguez & Gordillo 2020; Rodríguez-Díaz *et al.* 2023). Interestingly, the prediction for Newtonian liquids applies well to viscoelastic liquids by substituting Oh_p for Oh_s (figure 12b), particularly in the $De \rightarrow 0$ limit. Beyond $Oh_{p,c}$, the jet radius becomes ill defined as the jet gradually widens (figure 12a: $Oh_p = 0.035$), first reaching the dropping transition at $Oh_{p,d} \approx 0.048$ (figures 7 and 12b) and ultimately vanishing at $Oh_{p,j} \approx 0.129$ (figure 8b).

5. Conclusion and outlook

This work elucidates the effects of viscoelasticity on Worthington jet formation and droplet ejection, by contrasting it with Newtonian fluid behaviour. The process is governed by two key dimensionless parameters: the elastocapillary number Ec , comparing elastic and capillary forces, and the Deborah number De , relating the relaxation time of the polymeric liquid to the inertio-capillary time scale. We identify three distinct regimes in viscoelastic media, analogous to Newtonian fluids: (i) jet formation with droplet ejection, (ii) jets without droplets and (iii) complete jet suppression. However, the transitions between these regimes now depend on Ec and De rather than solely on the solvent Ohnesorge number Oh_s . Notably, while viscoelasticity significantly alters the jet dynamics, it does not affect the capillary wave speed.

Analysis across the Ec – De phase space reveals markedly different behaviours in two limiting cases. For polymeric liquids with permanent memory ($De \rightarrow \infty$), transitions occur at fixed Ec , independently of De . The jetting transition Ec_j is independent of Oh_s , while the dropping transition Ec_d exhibits strong Oh_s dependence. Remarkably, this infinite De asymptote extends down to $De \approx 1$, where the polymer relaxation time becomes comparable to the process time scale. Below this, for $De \sim \mathcal{O}(0.1)$, we observe a transition in scaling behaviour, consistent with the Weissenberg number

criterion $Wi \equiv De\sqrt{We_{jet}} \sim \mathcal{O}(1)$, where We_{jet} is the jet Weber number (4.8) that remains approximately constant due to negligible elastic effects during the initial shear flow (Blanco-Rodríguez & Gordillo 2021). Conversely, for polymeric liquids with poor memory ($De \rightarrow 0$), both transitions occur at constant polymeric Ohnesorge number $Oh_p = Ec \times De$, indicating that the addition of polymers introduces an excess viscous stress in this limit. These transitions are independent of Oh_s . Using a slender jet approach (Driessen *et al.* 2013; Eggers & Fontelos 2015; Gordillo *et al.* 2020), we provide further insights into these transitions, examining the competition between elastic stresses and inertial flow focusing that governs jet formation and droplet ejection. This analysis helps to explain the observed scaling behaviours and transition criteria.

Our findings have important implications for understanding and controlling bubble bursting in viscoelastic fluids, with relevance to biological processes (Walls *et al.* 2017), such as airborne disease transmission (Bourouiba 2021), and industrial applications, such as inkjet printing (Lohse 2022). The results highlight how polymer additives can dramatically alter spray formation, with intermediate values of Ec and De leading to smaller and faster droplets, whereas high values of Ec and De suppress droplet formation entirely (Kant *et al.* 2023). This work also opens several avenues for future research. Further investigation is needed into the universal behaviour near the infinite De asymptote, including the development of closed-form De expansions for free surface flows (Sen *et al.* 2021; Boyko *et al.* 2024; França *et al.* 2024; Hinch *et al.* 2024; Sen *et al.* 2024). The mechanism underlying the Oh_s sensitivity of transition Ec values at high De requires further clarification. Additionally, extending our analysis to nonlinear viscoelastic models would provide valuable insights into the role of shear-thinning behaviour and finite extensibility in bursting bubbles, addressing limitations of the current model (McKinley & Sridhar 2002; Snoeijer *et al.* 2020; Zinelis *et al.* 2024). This approach would allow quantification of discrepancies between experiments and simulations, often attributed to inherent issues with the Oldroyd-B model, thereby enhancing our understanding of viscoelastic jets (Gaillard *et al.* 2025). Indeed, the numerical method developed here, freely available in Sanjay & Dixit (2024), provides a generalised framework readily adaptable to any model within the Oldroyd-B family of upper convective derivative models (Snoeijer *et al.* 2020). Furthermore, as higher Bond numbers are observed in many scenarios (Ghabache, Séon & Antkowiak 2014; Walls *et al.* 2015; Krishnan *et al.* 2017; Deike *et al.* 2018), exploring their combined effect with viscoelasticity on the overall dynamics would provide valuable insights into such experiments (Rodríguez-Díaz *et al.* 2023). Indeed, a critical assumption of this work is the initial condition and flow history, particularly for bubbles at liquid–gas interfaces in viscoelastic or elastoviscoplastic media. Our current work assumes the bubble has resided at the interface for a duration far exceeding the polymeric medium’s relaxation time, ensuring elastic stresses have fully relaxed before bursting. This idealised scenario provides a well-defined starting point but may not fully capture experimental conditions (Chen & Walters 1996; Deoclecio, Soares & Popinet 2023). Lastly, studying interactions of multiple bubbles (Singh & Das 2019) at the liquid–gas free surface will provide further insights into pathogen transport.

Extensions of this work could also explore coated bubbles (Dollet, Marmottant & Garbin 2019; Yang *et al.* 2023) or those with surface elasticity (Ji *et al.* 2023), and incorporate surfactants that alter bulk or interfacial properties (Constante-Amores *et al.* 2021; Lohse 2022; Pierre, Poujol & Séon 2022; Pico *et al.* 2024). Utilising the current numerical framework to investigate the effects of bubble motion (Beris *et al.* 1985; Moschopoulos *et al.* 2021) and oscillations in viscoelastic media (Dollet *et al.* 2019;

Oratis *et al.* 2024) on the overall dynamics before bursting would also be beneficial. This model provides a general framework for studying both Newtonian viscous and non-Newtonian elastic effects. As a future perspective, it would be worthwhile to study phenomena such as wrinkling (Debrégeas *et al.* 1998; Oratis *et al.* 2020; Davidovitch & Klein 2024) and buckling (Le Merrer, Quéré & Clanet 2012; Timoshenko & Gere 2012), which occur in various viscoelastic systems (Schmalholz & Podladchikov 1999; Matoz-Fernandez *et al.* 2020; Lee & Dalnoki-Veress 2024). By encompassing both viscous and elastic behaviours, this approach enables a comprehensive study of these interconnected instabilities, elucidating their underlying mechanisms and relationships as envisioned by Stokes (1845), Lord Rayleigh (1896) and Taylor (1969). Moreover, integrating viscoelastic and elastoviscoplastic (Balasubramanian *et al.* 2024; França *et al.* 2024) properties into recently developed analytical methods for capillary wave propagation and convergence, such as those by Kayal *et al.* (2025), could yield a deeper theoretical understanding of the phenomenon.

In conclusion, this study investigates and characterises bubble bursting in viscoelastic media, interpreting the interplay between elastic, viscous and capillary forces by moving in the $Oh_s Ec-De$ phase space. As a starting point, we employed the Oldroyd-B constitutive model. While this choice elucidates the basic interplay of elasticity, viscosity and capillarity, it does not capture shear-thinning effects or finite extensibility of polymer chains. Therefore, the predicted droplet sizes, jet thinning dynamics and ultimate filament breakup must be interpreted with caution. More complex viscoelastic models (e.g. Giesekus, Finite Extensible Nonlinear Elastic-Peterlin (FENE-P)) that incorporate finite extensibility and nonlinearities will likely alter certain details of our findings. Hence, our results should be viewed as a conceptual road map rather than definitive predictions. An essential extension of our study involves the experimental validation of the numerical results. Controlled laboratory studies using polymer solutions with known rheological properties are needed to assess the accuracy of the Oldroyd-B model in this parameter regime (also see Appendix B). Such comparisons will help determine where the simplified assumptions fail and guide refinements, including the use of more realistic constitutive equations.

Despite these caveats, our study offers a foundation for understanding how viscoelasticity can either suppress or enhance droplet formation during bubble bursting. We hope this work will inspire future experiments and numerical explorations using more advanced rheological models, ultimately leading to a more complete and quantitative picture of viscoelastic bubble bursting across different application domains.

Supplementary movies. Supplementary movies are available at <https://doi.org/10.1017/jfm.2025.237>

Acknowledgements. We would like to thank A. Prosperetti, G. McKinley, J. Snoeijer, M. Jalaal, U. Sen and V. Bertin for discussions.

Funding. We acknowledge the funding from the MIST consortium. This publication is part of the project MIST with project number P20-35 of the research programme Perspectief, which is (partly) financed by the Dutch Research Council (NWO). We also acknowledge the NWO-Canon grant FIP-II grant. This work was carried out on the national e-infrastructure of SURFsara, a subsidiary of SURF cooperation, the collaborative ICT organization for Dutch education and research. This work was sponsored by NWO - Domain Science for the use of supercomputer facilities.

Declaration of interests. The authors report no conflict of interest.

Data availability. The codes used in the present article are permanently available in Sanjay & Dixit (2024).

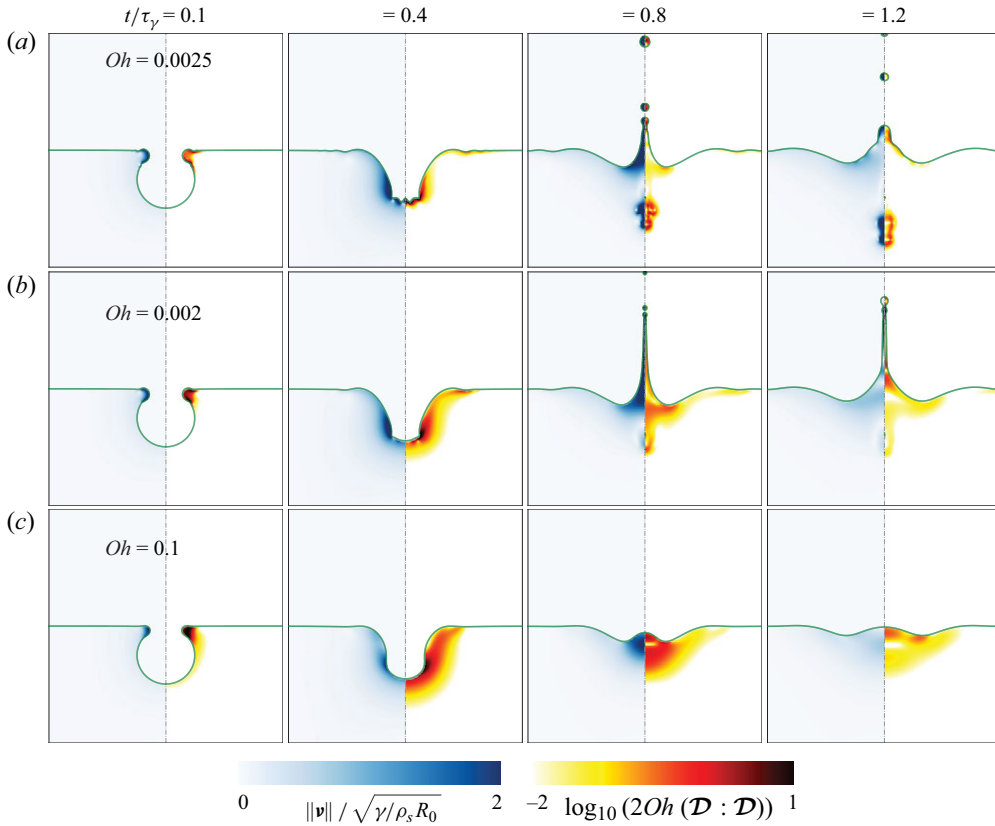


Figure 13. Temporal evolution of bubble cavity collapse in Newtonian liquid for $Oh_s = (a) 0.0025$, $(b) 0.02$ and $(c) 0.1$. The left panel represents the magnitude of the velocity field normalised by the inertio-capillary velocity, while the right panel shows the local viscous dissipation on a \log_{10} scale. See also the supplementary movies [SM3](#).

Appendix A. The Newtonian limit of bursting bubble dynamics

The dynamics of bursting bubbles in Newtonian media is solely dictated by the Ohnesorge number Oh_s in the limit of very small bubbles (Bond number $Bo \ll 1$). [Figure 13](#) illustrates representative cases at varying Oh_s for $Bo = 0.001$. At low Oh_s , capillary waves propagate along the cavity, converging at its base to form a Worthington jet that subsequently fragments into droplets ([figure 13a](#)). In this limit, multiple undamped capillary waves collide at the cavity's bottom, generating a thick Worthington jet. Increasing Oh_s dampens short-wavelength capillary waves, allowing the dominant wave to focus more effectively and produce a thinner jet. This explains the observed decrease in jet width with increasing Oh_s ([Gordillo & Blanco-Rodríguez 2023](#)), until a critical $Oh_c \approx 0.03$ (at $Bo = 0.001$) where the jet becomes extremely narrow, approaching a singularity ([Blanco-Rodríguez & Gordillo 2020](#)). Concurrently, the size of the first ejected droplet diminishes with increasing Oh_s ([Gordillo & Rodríguez-Rodríguez 2019](#)). As Oh_s further increases, bubble entrainment occurs. Beyond $Oh_{s,d} = 0.0375$, vertical droplet ejection ceases; instead, the jet undergoes Rayleigh–Plateau instability, producing droplets that fall back into the pool ([Walls *et al.* 2015](#); [Deike *et al.* 2018](#); [Blanco-Rodríguez & Gordillo 2020](#)). As Oh_s increases ($Oh_s > 0.045$), viscous dissipation becomes more prominent, resulting in jet formation without droplet ejection ([figure 13b](#)). Further increase

	c (ppm)	R (mm)	η_s (m pa s)	λ (μ s)	η_p (m pa s)	G (pa)
Chen & Walters (1996)	[0, 100]	7.5, 19	300	N/A	[0, 18]	N/A
Rodríguez-Díaz <i>et al.</i> (2023)	[0, 350]	1	1	[0, 500]	[0, 0.5]	[0, 1]
Cabalgante-corrales <i>et al.</i> (2025)	[0, 100]	0.93	0.89	[0, 700]	[0, 2]	[0, 1]

Table 1. Representative values of physical parameters in polymer solution studies from three representative works on the Worthington jets from the literature. Across these studies, the density of the medium and its surface tension coefficient are roughly 1000 kg/m³ and 70 mN/m, respectively. N/A represents unavailable data. See [table 2](#) for the estimates of dimensionless numbers using these properties.

	Oh_s	De	Ec	Oh_p	Bo
This work	$[10^{-3}, 10^0]$	$[0, \infty)$	$[0, 10^3]$	$[0, \infty)$	10^{-3}
Balasubramanian <i>et al.</i> (2024)	$[10^{-3}, 10^{-2}]$	$[0, 10^2]$	$[0, 10]$	$[10^{-3}, 10^{-2}]$	10^{-3}
Chen & Walters (1996)	10^{-1}	N/A	N/A	$[0, 10^{-2}]$	$[10, 10^2]$
Rodríguez-Díaz <i>et al.</i> (2023)	10^{-3}	$[0, 10^{-1}]$	$[0, 10^{-2}]$	$[0, 10^{-3}]$	10^{-1}
Cabalgante-Corrales <i>et al.</i> (2025)	10^{-3}	$[0, 2 \times 10^{-1}]$	$[0, 10^{-2}]$	$[0, 10^{-2}]$	10^{-1}

Table 2. Representative values of dimensionless numbers in this work as compared with those from previous studies. For experimental studies, the dimensionless parameters are calculated using the properties in [table 1](#). For Balasubramanian *et al.* (2024), we have only considered the limiting cases of zero yield stress. We note that while experiments are naturally limited in their accessible parameter ranges, our numerical study explores a broader range to establish comprehensive scaling laws and regime transitions.

in Oh_s beyond $Oh_{s,j} = 0.11$ completely suppresses jet formation (figure [13c](#), also see Sanjay *et al.* [2022](#)).

Appendix B. A note on the range of control parameters considered in this work

In this appendix, we tabulate and compare the range of dimensionless parameters explored in this work with those available in the literature on viscoelastic effects in bubble bursting. [Table 1](#) and [2](#) summarise the physical properties and corresponding dimensionless numbers from three representative experimental studies.

[Table 1](#) presents key physical parameters including polymer concentration (c), bubble radius (R), solvent viscosity (η_s), polymer relaxation time (λ), polymer contribution to viscosity (η_p) and elastic modulus (G). The corresponding dimensionless numbers are shown in [table 2](#), where we compare our parameter space with both experimental and computational studies from the literature. Our work systematically explores a significantly broader range of these parameters compared with experimental studies, which are often constrained by practical limitations in achievable polymer concentrations and relaxation times. This comprehensive coverage allows us to identify universal scaling laws and regime transitions that may be challenging to observe experimentally.

The ranges explored in our numerical study suggest several promising directions for future experimental investigations. For instance, while moving in the De - Ec parameter space, experiments could probe the robustness of our predicted transitions and scaling laws. Experimental studies would not only validate our computational findings but could also reveal additional physical mechanisms not captured by the Oldroyd-B model. We anticipate that trying new polymers and advances in characterisation techniques (Gaillard

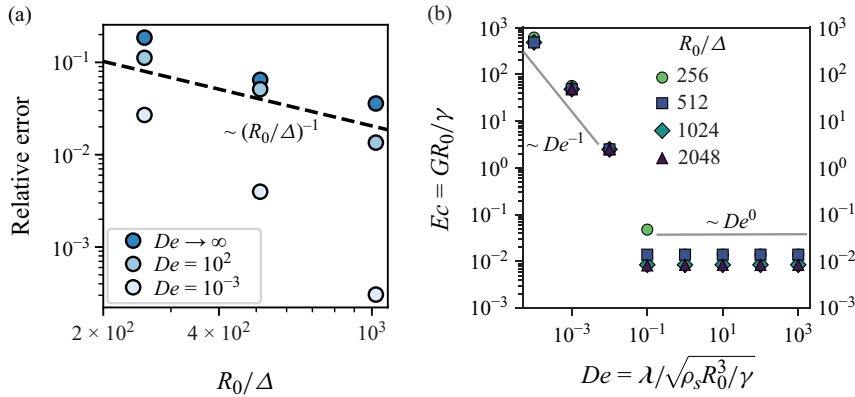


Figure 14. (a) The relative error in predicted droplet size versus the number of grid points per bubble radius, R_0/Δ , at $De \rightarrow \infty$, $De = 10^2$ and $De = 10^{-3}$. The dashed line indicates a scaling of $(R_0/\Delta)^{-1}$, demonstrating approximately first-order convergence for large De cases. The relative error for small De is lower as the elastic stresses are less prominent compared with large De . (b) Dependence of the critical elastocapillary number Ec_d at the dropping transition on the Deborah number De for different grid resolutions ($R_0/\Delta = 256, 512, 1024, 2048$). The scaling behaviours $Ec_d \sim De^{-1}$ as $De \rightarrow 0$ and $Ec_d \sim De^0$ as $De \rightarrow \infty$ remain unchanged beyond $R_0/\Delta = 1024$.

et al. 2024a) will continue to expand the experimentally accessible parameter space, enabling increasingly detailed comparisons between simulations and experiment.

Appendix C. Grid sensitivity tests

This appendix assesses the grid independence of our numerical results by examining two important metrics: (i) the predicted droplet size and (ii) the regime transitions. Ensuring grid convergence is crucial, especially if interface ruptures due to finite grid resolution in our numerical code (Lohse & Villerraux 2020; Chirco *et al.* 2022; Kant *et al.* 2023).

Figure 14(a) shows the relative error in predicted droplet size as a function of the number of grid points per initial bubble radius R_0/Δ , where Δ is the minimum grid size. We focus on $De \rightarrow \infty$ as this case is particularly demanding, featuring slender filaments due to viscoelastic stresses. The error is calculated relative to the finest resolution ($R_0/\Delta = 2048$). The data exhibit approximately first-order convergence, indicated by the dashed line scaling as $(R_0/\Delta)^{-1}$. For our standard resolution of $R_0/\Delta = 512$, the relative error is approximately 6 %, decreasing to approximately 3 % at $R_0/\Delta = 1024$.

While droplet size convergence demonstrates improved numerical accuracy with increasing resolution, the determination of regime transitions between different flow behaviours provides an even more stringent test. These transitions are highly sensitive to the details of jet breakup. Figure 14(b) displays the dimensionless elastocapillary number Ec at the transition boundary for different grid resolutions. We find that for $(R_0/\Delta) \geq 1024$, the transition curves do not change, confirming that the scaling behaviours previously identified – namely $Ec_d \sim De^{-1}$ for $De \ll 1$ and $Ec_d \sim De^0$ for $De \gg 1$ – are robustly reproduced across all grid resolutions tested.

Appendix D. Deviation from the Newtonian asymptote

In the main text, we showed that for small elastocapillary numbers Ec , the droplet size r_d and jet length L_{max} closely match those of the Newtonian case at arbitrary Oh_s (solvent

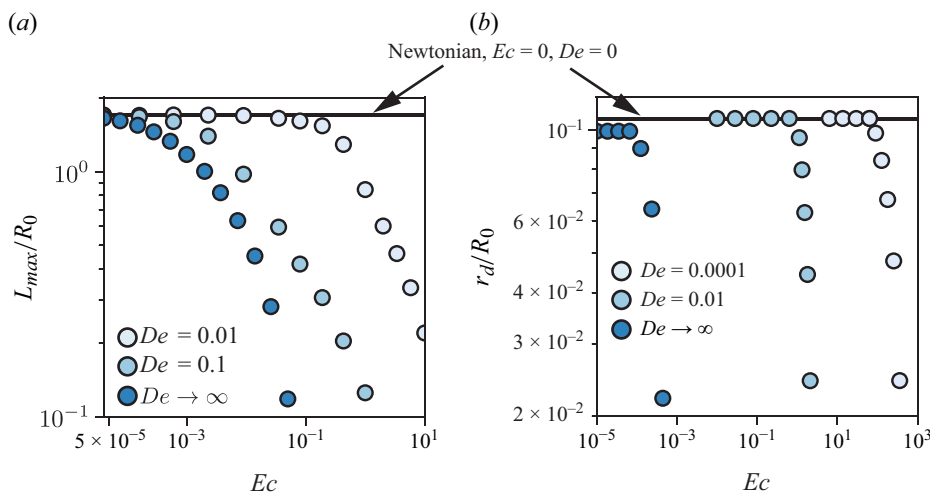


Figure 15. Comparison of (a) maximum jet length L_{max}/R_0 against Ec at various De at fixed representative cases of $Oh_s = 0.05$ and (b) first droplet size r_d/R_0 against Ec at various De fixed at $Oh_s = 0.001$. The horizontal lines indicate the Newtonian reference values (obtained at $Ec = 0$). At small Ec , both L_{max} and r_d coincide with their Newtonian counterparts, demonstrating negligible viscoelastic influence. As Ec increases beyond critical values, significant deviations from the Newtonian limits emerge, with the degree of departure depending on De . These results quantify the onset and magnitude of elastic effects relative to the Newtonian baseline, providing a clear framework for interpreting viscoelastic modifications to bursting bubble dynamics.

Ohnesorge number) and De (Deborah number). Only when Ec approaches or exceeds critical values do we observe significant departures from the Newtonian reference.

Figure 15 quantifies these deviations by comparing both the maximum jet length L_{max} (figure 15a) and the first droplet size r_d (figure 15b) against Ec at various De , in the limit of $Oh_s \ll 1$. The symbols represent numerical results for the viscoelastic system, while the horizontal lines mark the corresponding Newtonian asymptotes (i.e. r_d and L_{max} values obtained at $Ec = 0$). For small Ec , both r_d and L_{max} are invariant, indicating that viscoelastic stresses are negligible in this range. As Ec increases and approaches the critical thresholds identified in § 4, deviations emerge, ultimately leading to suppressed jetting or droplet formation.

Notably, the critical Ec value at which r_d and L_{max} deviate from their Newtonian counterparts depends on De . For high De , even a moderate increase in Ec can trigger significant changes, reflecting the persistent elastic memory in the fluid. In contrast, for $De \ll 1$, where the polymeric stresses relax rapidly, larger Ec values are necessary to produce noticeable departures from Newtonian behaviour. Similarly, the Newtonian limit is readily recovered by reducing either Ec or De to zero.

These results highlight that any interpretation of viscoelastic bubble-bursting dynamics should be framed with reference to the Newtonian baselines (either $De = 0$ or $Ec = 0$). By systematically mapping out these deviations, one can pinpoint the onset of non-Newtonian behaviour and interpret observed jetting or droplet formation regimes as outcomes of either weak or strong elastic effects, all benchmarked against the Newtonian scenario.

REFERENCES

- AFKHAM, S., BUONGIORNO, J., GUION, A., POPINET, S., SAADE, Y., SCARDOVELLI, R. & ZALESKI, S. 2018 Transition in a numerical model of contact line dynamics and forced dewetting. *J. Comput. Phys.* **374**, 1061–1093.

- ALVES, M.A., OLIVEIRA, P.J. & PINHO, F.T. 2021 Numerical methods for viscoelastic fluid flows. *Annu. Rev. Fluid Mech.* **53** (1), 509–541.
- ANNA, S.L. & MCKINLEY, G.H. 2001 Elasto-capillary thinning and breakup of model elastic liquids. *J. Rheol.* **45** (1), 115–138.
- BALASUBRAMANIAN, A.G., SANJAY, V., JALAAL, M., VINUESA, R. & TAMMISOLA, O. 2024 Bursting bubble in an elastoviscoplastic medium. *J. Fluid Mech.* **1001**, A9.
- BALCI, N., THOMASES, B., RENARDY, M. & DOERING, C.R. 2011 Symmetric factorization of the conformation tensor in viscoelastic fluid models. *J. Non-Newtonian Fluid Mech.* **166** (11), 546–553.
- BARTLETT, C., ORATIS, A.T., SANTIN, M. & BIRD, J.C. 2023 Universal non-monotonic drainage in large bare viscous bubbles. *Nat. Commun.* **14** (1), 877.
- BERGMANN, R., VAN DER MEER, D., GEKLE, S., VAN DER BOS, A. & LOHSE, D. 2009 Controlled impact of a disk on a water surface: cavity dynamics. *J. Fluid Mech.* **633**, 381–409.
- BERGMANN, R., VAN DER MEER, D., STIJNMAN, M., SANDTKE, M., PROSPERETTI, A. & LOHSE, D. 2006 Giant bubble pinch-off. *Phys. Rev. Lett.* **96** (15), 154505.
- BERIS, A.N., TSAMOPOULOS, J.A., ARMSTRONG, R.C. & BROWN, R.A. 1985 Creeping motion of a sphere through a Bingham plastic. *J. Fluid Mech.* **158**, 219–244.
- BERNY, A., DEIKE, L., SÉON, T. & POPINET, S. 2020 Role of all jet drops in mass transfer from bursting bubbles. *Phys. Rev. Fluids* **5** (3), 033605.
- BERNY, A., POPINET, S., SÉON, T. & DEIKE, L. 2021 Statistics of jet drop production. *Geophys. Res. Lett.* **48** (10), e2021GL092919.
- BERTIN, V., SANJAY, V., ORATIS, A.T. & SNOEIJER, J.H. 2024 Elastic Taylor–Culick retractions. Working paper.
- BIRD, R.B., DOTSON, P.J. & JOHNSON, N.L. 1980 Polymer solution rheology based on a finitely extensible bead–spring chain model. *J. Non-Newtonian Fluid Mech.* **7** (2-3), 213–235.
- BIRD, R.R., ARMSTRONG, R.C. & HASSAGER, O. 1977 In *Dynamics of Polymeric Liquids*, vol. 1, Fluid Mechanics. Wiley.
- BLANCO-RODRÍGUEZ, F.J. & GORDILLO, J.M. 2020 On the sea spray aerosol originated from bubble bursting jets. *J. Fluid Mech.* **886**, R2.
- BLANCO-RODRÍGUEZ, F.J. & GORDILLO, J.M. 2021 On the jets produced by drops impacting a deep liquid pool and by bursting bubbles. *J. Fluid Mech.* **916**, A37.
- BOGY, D.B. 1979 Drop formation in a circular liquid jet. *Annu. Rev. Fluid Mech.* **11** (1), 207–228.
- BOUILLANT, A., DEKKER, P.J., HACK, M.A. & SNOEIJER, J.H. 2022 Rapid viscoelastic spreading. *Phys. Rev. Fluids* **7** (12), 123604.
- BOULTON-STONE, J.M. & BLAKE, J.R. 1993 Gas bubbles bursting at a free surface. *J. Fluid Mech.* **254**, 437–466.
- BOUROUBA, L. 2021 The fluid dynamics of disease transmission. *Annu. Rev. Fluid Mech.* **53** (1), 473–508.
- BOUSFIELD, D.W., KEUNINGS, R., MARRUCCI, G. & DENN, M.M. 1986 Nonlinear analysis of the surface tension driven breakup of viscoelastic filaments. *J. Non-Newtonian Fluid Mech.* **21** (1), 79–97.
- BOYKO, E., HINCH, J. & STONE, H.A. 2024 Flow of an Oldroyd-B fluid in a slowly varying contraction: theoretical results for arbitrary values of Deborah number in the ultra-dilute limit. *J. Fluid Mech.* **988**, A10.
- BOYKO, E. & STONE, H.A. 2024 Perspective on the description of viscoelastic flows via continuum elastic dumbbell models. *J. Engng Maths* **147** (1), 1–18.
- BRACKBILL, J.U., KOTHE, D.B. & ZEMACH, C. 1992 A continuum method for modeling surface tension. *J. Comput. Phys.* **100** (2), 335–354.
- CABALGANTE-CORRALES, E., MUÑOZ-SÁNCHEZ, B.N., LÓPEZ-HERRERA, J.M., CABEZAS, M.G., VEGA, E.J. & MONTANERO, J.M. 2025 Effect of the polymer viscosity and relaxation time on the Worthington jet produced by bubble bursting in weakly viscoelastic liquids. *Intl J. Multiphase Flow* **184**, 105095.
- CHANG, H., DEMEKHIN, E.A. & KALADIN, E. 1999 Iterated stretching of viscoelastic jets. *Phys. Fluids* **11** (7), 1717–1737.
- CHEN, K. 1991 Interfacial instability due to elastic stratification in concentric coextrusion of two viscoelastic fluids. *J. Non-Newtonian Fluid Mech.* **40** (2), 155–175.
- CHENY, J.M. & WALTERS, K. 1996 Extravagant viscoelastic effects in the Worthington jet experiment. *J. Non-Newton. Fluid Mech.* **67**, 125–135.
- CHIRCO, L., MAAREK, J., POPINET, S. & ZALESKI, S. 2022 Manifold death: a volume of fluid implementation of controlled topological changes in thin sheets by the signature method. *J. Comput. Phys.* **467**, 111468.
- CLASEN, C., EGGERS, J., FONTELOS, M.A., LI, J. & MCKINLEY, G.H. 2006 The beads-on-string structure of viscoelastic threads. *J. Fluid Mech.* **556**, 283–308.

- CONSTANTE-AMORES, C.R., KAHOUADJI, L., BATCHVAROV, A., SHIN, S., CHERGUI, J., JURIC, D. & MATAR, O.K. 2021 Dynamics of a surfactant-laden bubble bursting through an interface. *J. Fluid Mech.* **911**, A57.
- CULICK, F.E.C. 1960 Comments on a ruptured soap film. *J. Appl. Phys.* **31** (6), 1128–1129.
- DANESHI, M. & FRIGAARD, I.A. 2024 Growth and static stability of bubble clouds in yield stress fluids. *J. Non-Newtonian Fluid Mech.* **327**, 105217.
- DASOUQI, A.A., GHOSSEIN, J. & MURPHY, D.W. 2022 The effect of liquid properties on the release of gas from bursting bubbles. *Exp. Fluids* **63** (1), 39.
- DAVIDOVITCH, B. & KLEIN, A. 2024 How viscous bubbles collapse: topological and symmetry-breaking instabilities in curvature-driven hydrodynamics. *Proc. Natl. Acad. Sci. USA* **121** (32), e2310195121.
- DAVOODI, M., LEROUGE, S., NOROUZI, M. & POOLE, R.J. 2018 Secondary flows due to finite aspect ratio in inertialess viscoelastic Taylor–Couette flow. *J. Fluid Mech.* **857**, 823–850.
- DE GENNES, P.-G. 1974 Coil-stretch transition of dilute flexible polymers under ultrahigh velocity gradients. *J. Chem. Phys.* **60** (12), 5030–5042.
- DE LEEUW, G., ANDREAS, E.L., ANGUELOVA, M.D., FAIRALL, C.W., LEWIS, E.R., O'DOWD, C., SCHULZ, M. & SCHWARTZ, S.E. 2011 Production flux of sea spray aerosol. *Rev. Geophys.* **49** (2), 2010RG000349.
- DEBRÉGEAS, G.D., DE GENNES, P.-G. & BROCHARD-WYART, F. 1998 The life and death of “bare” viscous bubbles. *Science* **279** (5357), 1704–1707.
- DEIKE, L. 2022 Mass transfer at the ocean–atmosphere interface: the role of wave breaking, droplets, and bubbles. *Annu. Rev. Fluid Mech.* **54** (1), 191–224.
- DEIKE, L., GHABACHE, E., LIGER-BELAIR, G., DAS, A.K., ZALESKI, S., POPINET, S. & SÉON, T. 2018 Dynamics of jets produced by bursting bubbles. *Phys. Rev. Fluids* **3** (1), 013603.
- DEKKER, P.J., HACK, M.A., TEWES, W., DATT, C., BOUILLANT, A. & SNOEIJER, J.H. 2022 When elasticity affects drop coalescence. *Phys. Rev. Lett.* **128** (2), 028004.
- DEOCLECIO, L.H.P., SOARES, E.J. & POPINET, S. 2023 Drop rise and interfacial coalescence initiation in Bingham materials. *J. Non-Newtonian Fluid* **319**, 105075.
- DOLLET, B., MARMOTTANT, P. & GARBIN, V. 2019 Bubble dynamics in soft and biological matter. *Annu. Rev. Fluid Mech.* **51** (1), 331–355.
- DRIESSEN, T.J., JEURISSEN, R., WIJSHOFF, H., TOSCHI, F. & LOHSE, D. 2013 Stability of viscous long liquid filaments. *Phys. Fluids* **25** (6), 062109.
- DUBITSKY, L., MCRAE, O. & BIRD, J.C. 2023a Enrichment of scavenged particles in jet drops determined by bubble size and particle position. *Phys. Rev. Lett.* **130** (5), 054001.
- DUBITSKY, L., STOKES, M.D., DEANE, G.B. & BIRD, J.C. 2023b Effects of salinity beyond coalescence on submicron aerosol distributions. *J. Geophys. Res. Atmos.* **128** (10), e2022JD038222.
- DUCHEMIN, L., POPINET, S., JOSSERAND, C. & ZALESKI, S. 2002 Jet formation in bubbles bursting at a free surface. *Phys. Fluids* **14** (9), 3000–3008.
- EGGERS, J. 1997 Nonlinear dynamics and breakup of free-surface flows. *Rev. Mod. Phys.* **69** (3), 865–930.
- EGGERS, J. & FONTELOS, M.A. 2015 *Singularities: Formation, Structure, and Propagation*. Vol. 53. Cambridge University Press.
- EGGERS, J.A., HERRADA, M.A. & SNOEIJER, J.H. 2020 Self-similar breakup of polymeric threads as described by the Oldroyd-B model. *J. Fluid Mech.* **887**, A19.
- EGGERS, J.H., SPRITTLES, J.E. & SNOEIJER, J. 2025 Coalescence dynamics. *Annu. Rev. Fluid Mech.* **57** (1), 61–87.
- FATTAL, R. & KUPFERMAN, R. 2004 Constitutive laws for the matrix-logarithm of the conformation tensor. *J. Non-Newtonian Fluid Mech.* **123** (2-3), 281–285.
- FRAGGEDAKIS, D., PAVLIDIS, M., DIMAKOPOULOS, Y. & TSAMOPOULOS, J. 2016 On the velocity discontinuity at a critical volume of a bubble rising in a viscoelastic fluid. *J. Fluid Mech.* **789**, 310–346.
- FRANÇA, H.L., JALAAL, M. & OISHI, C.M. 2024 Elasto-viscoplastic spreading: from plastocapillarity to elastocapillarity. *Phys. Rev. Res.* **6** (1), 013226.
- FULLANA, T., KULKARNI, Y., FRICKE, MATHIS, POPINET, S., AFKHAM, S., BOTHE, D. & ZALESKI, S. 2024 A consistent treatment of dynamic contact angles in the sharp-interface framework with the generalized Navier boundary condition, arXiv: 2411.10762. (Last accessed: March 19, 2025).
- GAILLARD, A., HERRADA, M.A., DEBLAIS, A., EGGERS, J. & BONN, D. 2024a Beware of CaBER: filament thinning rheometry does not always give ‘the’ relaxation time of polymer solutions. *Phys. Rev. Fluids* **9** (7), 073302.
- GAILLARD, A., HERRADA, M.A., DEBLAIS, A., VAN POELGEEST, C., LARUELLE, L., EGGERS, J. & BONN, D. 2025 When does the elastic regime begin in viscoelastic pinch-off? *J. Fluid Mech.* **1005**, A10.

- GAÑÁN-CALVO, A.M. 2017 Revision of bubble bursting: universal scaling laws of top jet drop size and speed. *Phys. Rev. Lett.* **119** (20), 204502.
- GHABACHE, É. & SÉON, T. 2016 Size of the top jet drop produced by bubble bursting. *Phys. Rev. Fluids* **1** (5), 051901.
- GHABACHE, É., SÉON, T. & ANTKOWIAK, A. 2014 Liquid jet eruption from hollow relaxation. *J. Fluid Mech.* **761**, 206–219.
- GIESEKUS, H. 1982 A simple constitutive equation for polymer fluids based on the concept of deformation-dependent tensorial mobility. *J. Non-Newtonian Fluid Mech.* **11** (1-2), 69–109.
- GONNERMANN, H.M. & MANGA, M. 2007 The fluid mechanics inside a volcano. *Annu. Rev. Fluid Mech.* **39** (1), 321–356.
- GORDILLO, J.M. & BLANCO-RODRÍGUEZ, F.J. 2023 Theory of the jets ejected after the inertial collapse of cavities with applications to bubble bursting jets. *Phys. Rev. Fluids* **8** (7), 073606.
- GORDILLO, J.M., ONUKI, H. & TAGAWA, Y. 2020 Impulsive generation of jets by flow focusing. *J. Fluid Mech.* **894**.
- GORDILLO, J.M. & RODRÍGUEZ-RODRÍGUEZ, J. 2019 Capillary waves control the ejection of bubble bursting jets. *J. Fluid Mech.* **867**, 556–571.
- GOREN, S.L. & GOTTLIEB, M. 1982 Surface-tension-driven breakup of viscoelastic liquid threads. *J. Fluid Mech.* **120**, 245–266.
- HINCH, E.J. 1993 The flow of an Oldroyd fluid around a sharp corner. *J. Non-Newtonian Fluid Mech.* **50** (2–3), 161–171.
- HINCH, J. & HARLEN, O. 2021 Oldroyd B, and not A? *J. Non-Newtonian Fluid Mech.* **298**, 104668.
- HINCH, J.E., BOYKO, E. & STONE, H.A. 2024 Fast flow of an oldroyd-b model fluid through a narrow slowly varying contraction. *J. Fluid Mech.* **988**, A11.
- HOSOKAWA, A., KAMAMOTO, K., WATANABE, H., KUSUNO, H., KOBAYASHI, K.U. & TAGAWA, Y. 2023 A phase diagram of the pinch-off-type behavior of impulsively-induced viscoelastic liquid jets. arXiv preprint arXiv: [2309.01364](https://arxiv.org/abs/2309.01364). (Last accessed: March 19, 2025).
- Ji, B., YANG, Z., WANG, Z., EWOLDT, R.H. & FENG, J. 2023 Secondary bubble entrainment via primary bubble bursting at a viscoelastic surface. *Phys. Rev. Lett.* **131** (10), 104002.
- KANT, P., PAIRETTI, C., SAADE, Y., POPINET, S., ZALESKI, S. & LOHSE, D. 2023 Bag-mediated film atomization in a cough machine. *Phys. Rev. Fluids* **8** (7), 074802.
- KAYAL, L., SANJAY, V., YEWALE, N., KUMAR, A. & DASGUPTA, R. 2025 Focusing of concentric free-surface waves. *J. Fluid Mech.* **1003**, A14.
- KELLER, J.B., KING, A. & TING, L. 1995 Blob formation. *Phys. Fluids* **7** (1), 226–228.
- KIENTZLER, C.F., ARONS, A.B., BLANCHARD, D.C. & WOODCOCK, A.H. 1954 Photographic investigation of the projection of droplets by bubbles bursting at a water surface. *Tellus* **6** (1), 1–7.
- KNELMAN, F., DOMBROWSKI, N. & NEWITT, D.M. 1954 Mechanism of the bursting of bubbles. *Nature* **173** (4397), 261–261.
- KRISHNAN, S., HOPFINGER, E.J. & PUTHENVEETIL, B.A. 2017 On the scaling of jetting from bubble collapse at a liquid surface. *J. Fluid Mech.* **822**, 791–812.
- LE MERRER, M., QUÉRÉ, D. & CLANET, C. 2012 Buckling of viscous filaments of a fluid under compression stresses. *Phys. Rev. Lett.* **109** (6), 064502.
- LEE, C.L. & DALNOKI-VERESS, K. 2024 Buckling instability in a chain of sticky bubbles. *Phys. Rev. Res.* **6** (2), L022062.
- LEE, J.S., WEON, B.M., PARK, S.J., JE, J.H., FEZZAA, K. & LEE, W.K. 2011 Size limits the formation of liquid jets during bubble bursting. *Nat. Commun.* **2** (1), 367.
- LHUISSIER, H. & VILLERMAUX, E. 2012 Bursting bubble aerosols. *J. Fluid Mech.* **696**, 5–44.
- LIGER-BELAIR, G. 2012 The physics behind the fizz in champagne and sparkling wines. *Eur. Phys. J. Spec. Topic* **201** (1), 1–88.
- LIN, T.J. 1970 Mechanisms and control of gas bubble formation in cosmetics. *J. Soc. Cosmet. Chem.* **22** (6), 323–337.
- LOHSE, D. 2003 Bubble puzzles. *Phys. Today* **56** (2), 36–41.
- LOHSE, D. 2018 Bubble puzzles: from fundamentals to applications. *Phys. Rev. Fluids* **3** (11), 110504.
- LOHSE, D. 2022 Fundamental fluid dynamics challenges in inkjet printing. *Annu. Rev. Fluid Mech.* **54** (1), 349–382.
- LOHSE, D., BERGMANN, R., MIKKELSEN, R., ZEILSTRA, C., VAN DER MEER, D., VERSLUIS, M., VAN DER WEELE, K., VAN DER HOEF, M. & KUIPERS, H. 2004 Impact on soft sand: void collapse and jet formation. *Phys. Rev. Lett.* **93** (19), 198003.
- LOHSE, D. & VILLERMAUX, E. 2020 Double threshold behavior for breakup of liquid sheets. *Proc. Natl. Acad. Sci. USA* **117** (32), 18912–18914.

- LÓPEZ-HERRERA, J.-M., POPINET, S. & CASTREJÓN-PITA, A.-A. 2019 An adaptive solver for viscoelastic incompressible two-phase problems applied to the study of the splashing of weakly viscoelastic droplets. *J. Non-Newtonian Fluid Mech.* **264**, 144–158.
- RAYLEIGH, LORD 1878 On the instability of jets. *Proc. Lond. Math. Soc.* **1** (1), 4–13.
- LORD, R. 1896 *The Theory of Sound*. Dover.
- MACINTYRE, F. 1972 Flow patterns in breaking bubbles. *J. Geophys. Res.* **77** (27), 5211–5228.
- MARCHAND, A., WEIJS, J.H., SNOEIJER, J.H. & ANDREOTTI, B. 2011 Why is surface tension a force parallel to the interface? *Am. J. Phys.* **79** (10), 999–1008.
- MASON, B.J. 1954 Bursting of air bubbles at the surface of sea water. *Nature* **174** (4427), 470–471.
- MATHIJSEN, A.J.T.M., LISICKI, M., PRAKASH, V.N. & MOSSIGE, E.J.L. 2023 Culinary fluid mechanics and other currents in food science. *Rev. Mod. Phys.* **95** (2), 025004.
- MATÓZ-FERNÁNDEZ, D.A., DAVIDSON, F.A., STANLEY-WALL, N.R. & SKNEPNEK, R. 2020 Wrinkle patterns in active viscoelastic thin sheets. *Phys. Rev. Res.* **2** (1), 013165.
- MCKINLEY, G.H. & SRIDHAR, T. 2002 Filament-stretching rheometry of complex fluids. *Annu. Rev. Fluid Mech.* **34** (1), 375–415.
- MIDDLEMAN, S. 1965 Stability of a viscoelastic jet. *Chem. Engng Sci.* **20** (12), 1037–1040.
- MOSCHOPOULOS, P., SPYRIDAKIS, A., VARCHANIS, S., DIMAKOPOULOS, Y. & TSAMOPOULOS, J. 2021 The concept of elasto-visco-plasticity and its application to a bubble rising in yield stress fluids. *J. Non-Newtonian Fluid Mech.* **297**, 104670.
- MUNRO, J. 2019 Coalescence of bubbles and drops. *PhD thesis*, University of Cambridge.
- OLDROYD, J.G. 1950 On the formulation of rheological equations of state. *Proc. R. Soc. Lond.* **200** (1063), 523–541.
- ORATIS, A.T., BERTIN, V. & SNOEIJER, J.H. 2023 Coalescence of bubbles in a viscoelastic liquid. *Phys. Rev. Fluids* **8** (8), 083603.
- ORATIS, A.T., BUSH, J.W.M., STONE, H.A. & BIRD, J.C. 2020 A new wrinkle on liquid sheets: turning the mechanism of viscous bubble collapse upside down. *Science* **369** (6504), 685–688.
- ORATIS, A.T., DIJS, K., LAJOINIE, G., VERSLUIS, M. & SNOEIJER, J.H. 2024 A unifying Rayleigh–Plesset-type equation for bubbles in viscoelastic media. *J. Acoust. Soc. Am.* **155** (2), 1593–1605.
- PANDEY, A., KANSAL, M., HERRADA, M.A., EGGERS, J. & SNOEIJER, J.H. 2021 Elastic Rayleigh–Plateau instability: dynamical selection of nonlinear states. *Soft Matt.* **17** (20), 5148–5161.
- PICO, P.P., KAHOUADJI, L.L., SHIN, S.S., CHERGUI, J.J., JURIC, D.D. & MATAR, O.K. 2024 Drop encapsulation and bubble bursting in surfactant-laden flows in capillary channels. *Phys. Rev. Fluids* **9** (3), 034001.
- PIERRE, J., POUJOL, M. & SÉON, T. 2022 Influence of surfactant concentration on drop production by bubble bursting. *Phys. Rev. Fluids* **7** (7), 073602.
- PLATEAU, J.A.F. 1873 *Statique expérimentale et théorique des liquides soumis aux seules forces moléculaires: Tome premier*. Vol. 2, Gauthier–Villars.
- POPINET, S. 2009 An accurate adaptive solver for surface-tension-driven interfacial flows. *J. Comput. Phys.* **228** (16), 5838–5866.
- POPINET, S. 2015 A quadtree-adaptive multigrid solver for the Serre–Green–Naghdi equations. *J. Comput. Phys.* **302**, 336–358.
- POPINET, S. 2018 Numerical models of surface tension. *Annu. Rev. Fluid Mech.* **50** (1), 49–75.
- POPINET, S. & collaborators 2013–2024 Basilisk C. <http://basilisk.fr> (Last accessed: June, 2024)
- PRINCEN, H.M. 1963 Shape of a fluid drop at a liquid–liquid interface. *J. Colloid Sci.* **18** (2), 178–195.
- PUTZ, A.M.V. & BURGHELEA, T.I. 2009 The solid–fluid transition in a yield stress shear thinning physical gel. *Rheol. Acta* **48** (6), 673–689.
- REMMELGAS, J., SINGH, P. & LEAL, L.G. 1999 Computational studies of nonlinear elastic dumbbell models of Boger fluids in a cross-slot flow. *J. Non-Newtonian Fluid Mech.* **88** (1–2), 31–61.
- RENARDY, M. & THOMASES, B. 2021 A mathematician’s perspective on the oldroyd b model: progress and future challenges. *J. Non-Newtonian Fluid Mech.* **293**, 104573.
- RODRÍGUEZ-DÍAZ, P., RUBIO, A., MONTANERO, J.M., GAÑÁN-CALVO, A.M. & CABEZAS, M.G. 2023 Bubble bursting in a weakly viscoelastic liquid. *Phys. Fluids* **35** (10), 102107.
- SANJAY, V. 2022 Viscous free-surface flows. *PhD thesis*, University of Twente.
- SANJAY, V. 2024 Code repository: Basilisk C ElastoFlow – Complete 2D/3D viscoelastic framework, <https://doi.org/10.5281/zenodo.14210635>. (Last accessed: March 19, 2025).
- SANJAY, V. & DIXIT, A.K. 2024 Code repository: viscoelastic Worthington jets & droplets produced by bursting bubbles, <https://doi.org/10.5281/zenodo.14349207>. (Last accessed: March 19, 2025).
- SANJAY, V., LOHSE, D. & JALAAL, M. 2021 Bursting bubble in a viscoplastic medium. *J. Fluid Mech.* **922**, A2.

- SANJAY, V., SEN, U., KANT, P. & LOHSE, D. 2022 Taylor–Culick retractions and the influence of the surroundings. *J. Fluid Mech.* **948**, A14.
- SARAMITO, P. 2007 A new constitutive equation for elastoviscoplastic fluid flows. *J. Non-Newtonian Fluid Mech.* **145** (1), 1–14.
- SCHMALHOLZ, S.M. & PODLADCHIKOV, Y. 1999 Buckling versus folding: Importance of viscoelasticity. *Geophys. Res. Lett.* **26** (17), 2641–2644.
- SEN, U., DATT, C., SEGERS, T., WIJSHOFF, H., SNOEIJER, J.H., VERSLUIS, M. & LOHSE, D. 2021 The retraction of jetted slender viscoelastic liquid filaments. *J. Fluid Mech.* **929**, A25.
- SEN, U., LOHSE, D. & JALAAL, M. 2024 Elastocapillary worthington jets. arXiv preprint arXiv: [2207.07928](https://arxiv.org/abs/2207.07928). (Last accessed: March 19, 2025).
- SHI, X.D., BRENNER, M.P. & NAGEL, S.R. 1994 A Cascade of structure in a drop falling from a faucet. *Science* **265** (5169), 219–222.
- SINGH, D. & DAS, A.K. 2019 Numerical investigation of the collapse of a static bubble at the free surface in the presence of neighbors. *Phys. Rev. Fluids* **4** (2), 023602.
- SINGH, D. & DAS, A.K. 2021 Dynamics of inner gas during the bursting of a bubble at the free surface. *Phys. Fluids* **33** (5), 052105.
- SNOEIJER, J.H., PANDEY, A., HERRADA, M.A. & EGGERS, J. 2020 The relationship between viscoelasticity and elasticity. *Proc. R. Soc. A* **476** (2243), 20200419.
- STOKES, G.G. 1845 On the theories of the internal friction of fluids in motion, and of the equilibrium and motion of elastic solids. *Trans. Camb. Philos. Soc.* **8**, 287.
- STONE, H.A. & LEAL, L.G. 1989 Relaxation and breakup of an initially extended drop in an otherwise quiescent fluid. *J. Fluid Mech.* **198**, 399–427.
- STONE, H.A., SHELLEY, M.J. & BOYKO, E. 2023 A note about convected time derivatives for flows of complex fluids. *Soft Matt.* **19** (28), 5353–5359.
- STUHLMAN, O.Jr 1932 The mechanics of effervescence. *Physics* **2** (6), 457–466.
- TANNER, R.I. 2000 *Engineering Rheology*. Vol. 52. OUP Oxford.
- TAYLOR, G.I. 1959 The dynamics of thin sheets of fluid III. Disintegration of fluid Sheets. *Proc. R. Soc. Lond.* **253**, 313–321.
- TAYLOR, G.I. 1969 Instability of jets, threads, and sheets of viscous fluid. In *Proceedings of the Twelfth International Congress of Applied Mechanics, Stanford*, pp. 382–388. Springer.
- TIMOSHENKO, S.P. & GERE, J.M. 2012 *Theory of Elastic Stability*. Courier Corporation.
- TOBA, Y. 1959 Drop production by bursting of air bubbles on the sea surface (ii) theoretical study on the shape of floating bubbles. *J. Oceanogr. Soc. Japan* **15** (3), 121–130.
- TROUTON, F.T. 1906 On the coefficient of viscous traction and its relation to that of viscosity. *Proc. R. Soc. Lond.* **77** (519), 426–440.
- TRYGGVASON, G., SCARDOVELLI, R. & ZALESKI, S. 2011 *Direct Numerical Simulations of Gas–Liquid Multiphase Flows*. Cambridge University Press.
- TURKOZ, E., LOPEZ-HERRERA, J.M., EGGERS, J., ARNOLD, C.B. & DEIKE, L. 2018 Axisymmetric simulation of viscoelastic filament thinning with the Oldroyd-B model. *J. Fluid Mech.* **851**, R2.
- TURKOZ, E., STONE, H.A., ARNOLD, C.B. & DEIKE, L. 2021 Simulation of impulsively induced viscoelastic jets using the Oldroyd-B model. *J. Fluid Mech.* **911**, A14.
- VARCHANIS, S., MAKRIGIORGOS, G., MOSCHOPOULOS, P., DIMAKOPOULOS, Y. & TSAMOPOULOS, J. 2019 Modeling the rheology of thixotropic elasto-visco-plastic materials. *J. Rheol.* **63** (4), 609–639.
- VARCHANIS, S. & TSAMOPOULOS, J. 2022 Numerical simulations of interfacial and elastic instabilities. *Sci. Talks* **3**, 100053.
- VILLERMAUX, E., WANG, X. & DEIKE, L. 2022 Bubbles spray aerosols: Certitudes and mysteries. *Proc. Natl. Acad. Sci. Nexus* **1** (5), pgac261.
- WALLS, P.L.L., HENAU, L. & BIRD, J.C. 2015 Jet drops from bursting bubbles: how gravity and viscosity couple to inhibit droplet production. *Phys. Rev. E* **92** (2), 021002.
- WALLS, P.L.L., MCRAE, O., NATARAJAN, V., JOHNSON, C., ANTONIOU, C. & BIRD, J.C. 2017 Quantifying the potential for bursting bubbles to damage suspended cells. *Sci. Rep.* **7** (1), 15102.
- WOODCOCK, A.H., KIENTZLER, C.F., ARONS, A.B. & BLANCHARD, D.C. 1953 Giant condensation nuclei from bursting bubbles. *Nature* **172** (4390), 1144–1145.
- WORTHINGTON, A.M. 1877 On the forms assumed by drops of liquids falling vertically on a horizontal plate. *Proc. R. Soc. Lond.* **25** (171–178), 261–272.
- WORTHINGTON, A.M. 1908 *A Study of Splashes*. Longman, Green and Co.
- YAMANI, S. & MCKINLEY, G.H. 2023 Master curves for FENE-P fluids in steady shear flow. *J. Non-Newtonian Fluid Mech.* **313**, 104944.

- YANG, Z., JI, B., AULT, J.T. & FENG, J. 2023 Enhanced singular jet formation in oil-coated bubble bursting. *Nat. Phys.* **19** (6), 884–890.
- YANG, Z.Q., TIAN, Y.S. & THORODDSEN, S.T. 2020 Multitude of dimple shapes can produce singular jets during the collapse of immiscible drop-impact craters. *J. Fluid Mech.* **904**, A19.
- YARIN, A.L. 1993 *Free Liquid Jets and Films: Hydrodynamics and Rheology*. Longman Scientific and Technical.
- ZEFF, B.W., KLEBER, B., FINEBERG, J. & LATHROP, D.P. 2000 Singularity dynamics in curvature collapse and jet eruption on a fluid surface. *Nature* **403** (6768), 401–404.
- ZINELIS, K., ABADIE, T., MCKINLEY, G.H. & MATAR, O.K. 2024 Transition to elasto-capillary thinning dynamics in viscoelastic jets. *J. Fluid Mech.* **998**, A4.